

The fault plane as the main fluid pathway

Geothermal field development options under subsurface and operational uncertainty

Daniilidis, Alexandros; Saeid, Sanaz ; Gholizadeh Doonechaly, Nima

DOI

[10.1016/j.renene.2021.02.148](https://doi.org/10.1016/j.renene.2021.02.148)

Publication date

2021

Document Version

Final published version

Published in

Renewable Energy

Citation (APA)

Daniilidis, A., Saeid, S., & Gholizadeh Doonechaly, N. (2021). The fault plane as the main fluid pathway: Geothermal field development options under subsurface and operational uncertainty. *Renewable Energy*, 171, 927-946. <https://doi.org/10.1016/j.renene.2021.02.148>

Important note

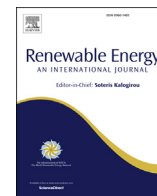
To cite this publication, please use the final published version (if applicable). Please check the document version above.

Copyright

Other than for strictly personal use, it is not permitted to download, forward or distribute the text or part of it, without the consent of the author(s) and/or copyright holder(s), unless the work is under an open content license such as Creative Commons.

Takedown policy

Please contact us and provide details if you believe this document breaches copyrights. We will remove access to the work immediately and investigate your claim.



The fault plane as the main fluid pathway: Geothermal field development options under subsurface and operational uncertainty

Alexandros Daniilidis ^{a,b,*}, Sanaz Saeid ^a, Nima Gholizadeh Doonechaly ^c

^a Delft University of Technology, Faculty of Civil Engineering and Geoscience, Petroleum Engineering, Stewinweg 1, Delft, 2628CN, the Netherlands

^b University of Geneva, Faculty of Science, Reservoir Geology and Basin Analysis, Rue des Maraichers 13, 1205, Geneva, Switzerland

^c ETH Zurich, Department of Earth Sciences, Sonneggstrasse 5, 8092, Zurich, Switzerland



ARTICLE INFO

Article history:

Available online 2 March 2021

Keywords:

Fault anisotropy

Uncertainty

System lifetime

NPV

Field development

Reservoir simulation

ABSTRACT

Geothermal energy is gaining momentum as a renewable energy source. Reservoir simulation studies are often used to understand the underlying physics interactions and support decision making. Uncertainty related to geothermal systems can be substantial for subsurface and operational parameters and their interaction with regards to the output in terms of lifetime, energy and economic output. Specifically, for geothermal systems with the fault acting as the main fluid pathway the relevant field development uncertainties have not been comprehensively addressed. In this study we show how the produced energy, system lifetime and NPV are affected considering a range of subsurface and operational parameters as uncertainty sources utilizing an ensemble of 16,200 3D Hydraulic-Thermal (HT) reservoir simulations, conceptually based on the Rittershoffen field. A well configuration with oblique angles with respect to the main permeability anisotropy axes results in higher system lifetime, generated energy and NPV. A well spacing of 600 m consistently yields a higher economic efficiency (€/MWh) under all uncertainty parameters considered. More robust development options could be utilized in the absence of fault permeability characterization to ensure improved output prediction under uncertainty. Studies based on the methodology presented can improve investment efficiency for field development under subsurface and operational uncertainty.

© 2021 The Author(s). Published by Elsevier Ltd. This is an open access article under the CC BY-NC-ND license (<http://creativecommons.org/licenses/by-nc-nd/4.0/>).

1. Introduction

Geothermal energy is increasingly considered as a renewable energy source to provide both electricity and heat. Improving system lifetime, energy generation and economic efficiency is crucial for a larger contribution of geothermal energy in the energy mix. Similar to other subsurface developments, such as in hydrocarbon reservoirs and CO₂ sequestration [1,2], an efficient well placement and configuration strategy is of crucial importance in geothermal reservoirs, in particular for Enhanced Geothermal Systems (EGS) due to their long borehole length. A significant portion of the capital costs for the exploitation of subsurface resources is allocated to well drilling. An appropriate well placement strategy can remarkably improve the reservoir performance and its economic

feasibility [3–7]. In this study we investigate the use of a fault plane as the main reservoir and show how the produced energy, system lifetime and NPV are affected considering uncertainty in both the subsurface and operational parameters.

An efficient well placement strategy requires detailed information about the reservoir's structure, geometry, petrophysical and hydrothermal-properties [8]. Spatial distribution of reservoir properties can affect the fluid flow pattern over different scales. In the cases of re-injection- and/or multiple-wells in geothermal reservoirs the relative position of the wells plays a major role in the success of the project [7,9,10]. Larger well spacing results in increased life time of the reservoir (due to prolonged thermal breakthrough time) and increased extracted energy, however, capital- and operational-costs for pipeline construction and pumping requirements will increase respectively [7,11–15]. This is especially important when considering the relatively low profit margin of geothermal projects for direct use of heat [16–18]. Additionally, energy required for pumping differs according to the flow properties of the target reservoir [19].

The existence of preferential flow paths, such as fault and/or

* Corresponding author. Delft University of Technology, Faculty of Civil Engineering and Geoscience, Reservoir Engineering, Stewinweg 1, Delft, 2628CN, the Netherlands.

E-mail address: a.daniilidis@tudelft.nl (A. Daniilidis).

fractures, especially in EGS, can significantly influence the well placement strategy [20–24]. Faults or fault zones can often form effective fluid pathways that naturally enhance the thermal gradient and fluid flow [25,26]. Faults as fluid pathways are more often targeted in low-permeability, basement rocks [27] or artificially generated by stimulation in EGS systems [28]. For example, it was observed that the targeted fault zone in Rittershoffen geothermal reservoir controls two third of the total flow within the system [29,30]. When faults are the main fluid pathways for fluid circulation the characterisation of permeability and permeability anisotropy directions are crucial for productivity [25,31] and the well configuration has been shown to affect the performance [32].

The well placement strategy is not only influenced by subsurface uncertainties, but also by future operational conditions which can complicate development options. Additionally to subsurface uncertainty, operational conditions can also influence the well placement strategy [33,34]. For example—in the context of a profitability analysis of the Soultz-sous-Forêts- EGS— it has been shown that the thermal breakthrough time of the system can be significantly influenced by the Rayleigh number, as well as by the flow rate and therefore, the operational conditions can indirectly affect the well placement strategy [35]. Non-isothermal effects add to the complexity of the selection of a suitable wellbore location in geothermal systems. In such systems, the variation in fluid density due to temperature change generates a buoyancy force ([36]; [37]). Buoyancy driven flow can reduce the pumping requirements or even eliminate the need for pumping between the injection and production wells if utilized appropriately [38]. In order to efficiently utilize the buoyancy effects, however, an appropriate well placement strategy is one of the most important requirements [39,40]. Additionally, it has been shown that in the presence of strong buoyancy effects in fractured geothermal systems the sweep efficiency of the heat inside the fractures is significantly influenced if the production well lies vertically above the injector well [38,41,42].

Besides the well placement itself, the producing interval of the wellbore within the reservoir section may also influence the overall performance of geothermal systems [43]. A full wellbore perforation decreases the pressure impedance, while perforating only the lower reservoir parts improves the production temperature in horizontal and homogeneous reservoirs [44]. Similarly, in a layered reservoir, higher permeability for the deeper layers yields increased produced fluid temperature [7]. However, in an inclined reservoir that could resemble a dipping fault the choice of production well location becomes very important and depends on the reservoir dip and initial thermal gradient [15].

Therefore, the different well spacing and positioning, together with the operational parameters affect both the generated energy and the economic performance of geothermal systems [14,17,45,46]. Moreover, drilling costs are associated with lithology, but also with well trajectory and have been shown to strongly correlate to measured depth [47,48]. Field development analysis has been carried out for direct use geothermal systems with formations as the fluid pathway, however, such an analysis is notably lacking for systems with fault as the main fluid pathway. The interaction between subsurface uncertainty and development options for fault-based systems has not been addressed previously.

The aim of this investigation is to determine the influence of the relative positioning of the wells, their spacing and the producing interval on the overall performance of a typical geothermal reservoir with the fault plane acting as the main fluid pathway. The performance of the geothermal system in terms of lifetime, amount of produced energy and generated NPV is analysed with respect to reservoir and operational uncertainty parameters, namely, flow rate, injection fluid temperature, fault permeability anisotropy and subsurface geothermal gradient. This study explores such an

interrelationship in the form of a sensitivity analysis, taking into account all discrete combinations of the above-mentioned parameters in a full factorial design study, comprised of 16,200 simulations. The modelled system conceptually represents the Rittershoffen geothermal reservoir (NE France). A numerical Thermal Hydraulic (TH) model employing the Finite Element Method (FEM) in COMSOL Multiphysics is used to perform the simulations.

2. Model

The model geometry and the inputs (section 2.1) of the parametric study are described first (section 2.2). Following, the three parts of the model are detailed: the reservoir model (section 2.3), coupling, initial and boundary conditions (section 2.4) and lastly the energy and economic model (section 2.5).

2.1. Model geometry and inputs

The proposed sensitivity analysis is based on the Rittershoffen geothermal reservoir and a numerical model is constructed based on the publicly available data. The reservoir consists of altered/fractured granitic rocks of Carboniferous age. It is located at the western part of the Upper Rhine Graben (URG), 6 km south-east of Soultz-sous-Forêts EGS [30]. The constructed numerical model consists of five layers in total (Fig. 1), representing (I) Lias, (II) Keuper-, (III) Muschelkalk- and (IV) Buntsandstein-formations as well as (V) the targeted granitic section [30,49,50]. The main damage zone of the fault in the region (Rittershoffen fault) has a thickness of 40m, a strike angle of N355° (becoming North-South at the granitic reservoir) and a dip angle of 45° to the West [30]. For simplicity, the fault strike is assumed to be North-South in the

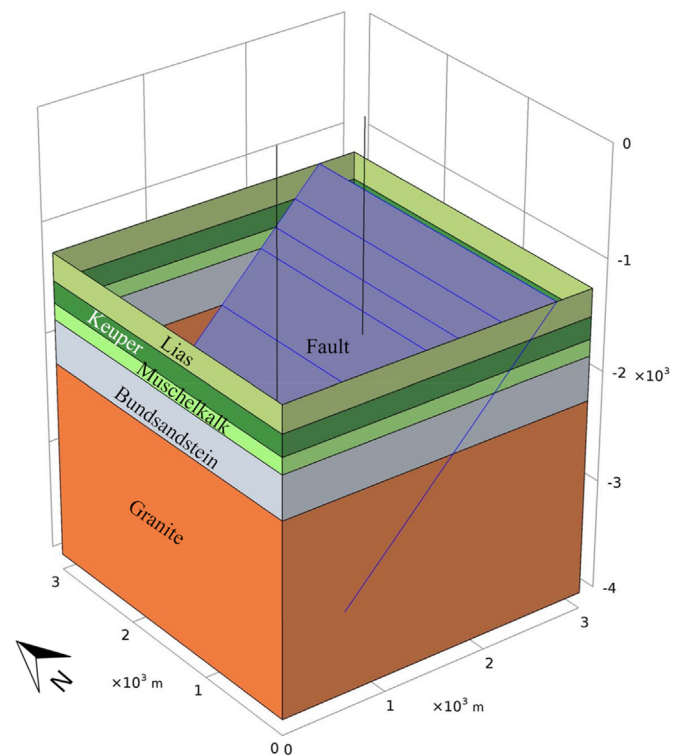


Fig. 1. Constructed reservoir model, including the Rittershoffen fault (presented in blue colour) as well as the production well (West) and injection well (East). The model layers (from top to bottom) represent: Lias, Keuper, Muschelkalk, Buntsandstein and the granitic section, respectively. Injection and production wells are treated as 1D line elements.

current study. The fault terminates at the true vertical depth of 3250m [30]. In order to target the fault zone, an injection-as well as a production-well are placed vertically in the model. The wells properties, such as location and depth, will be assigned based on every specific parametric value set. In the Rittershoffen geothermal field both wells are fully perforated inside the Muschelkalk, Bundsandstein, and partially penetrating granite (up to 150 m below the fault zone). In this study in order to investigate the effect of perforation length, both full perforation length (as exist in the Rittershoffen field) and partial perforation are studied. Partial perforation is implemented as 150 m above and below fault intersection with any reservoir layer.

A schematic representation of a typical built model including the Rittershoffen fault, as well as the injection/production wells—which in this particular case are positioned along the EW direction—is shown in Fig. 1. The properties of the granitic section of the reservoir are assigned based on the acquired data from the boreholes GRT-1 and GRT-2 in the Rittershoffen reservoir which were drilled in 2012 and 2014 respectively [30]. The model parameters for the layers above the granitic reservoir are set according to the analogue data [51; 52]. In cases of data not being publicly available, assumptions are made. The set of all model parameters are presented in Table 1. No flow is assumed for all outer boundaries of the model. The subsurface heat flux of 0.12W/m² is applied to the bottom surface of the model [53]. The subsurface temperature gradient is set at 0.09K/m for the layers above the Muschelkalk. The thermal gradient of the Muschelkalk and the lower layers are set according to the parametric sensitivity analysis (see section 2.2).

2.2. Full factorial parametric study

In order to carry out the sensitivity analysis, the wells relative position, well spacing, injection/production flow rate, injection temperature, fault permeability, fault permeability anisotropy, perforation length and subsurface geothermal gradient inside the Muschelkalk and the lower layers are changed according to typical ranges available in the literature (see Table 2). The simulation is carried out in the reservoir for every case study for a period of 100 years. The hydro-thermal behaviour of the system, including the thermal front propagation, produced fluid temperature/pressure and the produced thermal power are monitored. These will be consequently compiled into required pumping energy, produced energy and system lifetime. The list of all properties and their corresponding values are presented in Table 2.

2.3. Reservoir model

Modelling deep geothermal systems involves solving nonlinear conductive-convective heat flow occurring in a complicated and disproportionate geometry. In the Rittershoffen geothermal reservoir due to the fault stimulation the main fluid flow and heat transfer occurs through the fault. To model this geothermal reservoir in the most computational efficient way, the reservoir model is

decomposed in 3 parts; a 3D heat and fluid flow model in porous media, a 2D heat and fluid flow model in fault and a 1D heat and fluid flow model inside wellbores. The model domain has dimensions of 3 km (Northing) × 3 km (Easting) × 3 km (Depth).

Because of the low thickness of the fault compared with the large scale model and in order to improve the computational efficiency [23,54], the fault is modelled in 2D as a lower dimension element. The wellbore is a highly slender cylinder consisting of an inner pipe carrying the fluid, surrounded by a cemented grout and soil mass. Such geometry exhibits a unique and challenging numerical problem. If a standard 3D finite element (finite volume or finite difference) formulation is utilized to model heat flow in the wellbore and the surrounding soil mass, meshes with an enormous number of finite elements will be needed, resulting in unrealistic computational time [55, 15]. To decrease the computational demands a pseudo-3D model is considered for wellbore modelling. This model is capable of simulating heat flow in a multicomponent domain using a 1D line element [55–57].

2.3.1. Heat and fluid flow in the reservoir

Heat and fluid flow in the reservoir can be explained by Energy Balance and Darcy equations as:

$$\rho C \frac{\partial T}{\partial t} + \rho_f C_f q \nabla T - \nabla \cdot (\lambda \nabla T) = 0 \tag{1}$$

where T (K) is the temperature, ρ is the mass density (kg/m³), c (J/kg.K) is the specific heat capacity, λ (W/m.K) is the thermal conductivity, and **q** (m/s) is the Darcy velocity. The suffix *f* refers to the pore fluid and *s* to the solid matrix. The thermal conductivity and the volumetric heat capacity are described in terms of a local volume average, as

$$\lambda = (1 - \phi) \lambda_s + \phi \lambda_f \tag{2}$$

$$\rho C = (1 - \phi) \rho_s C_s + \phi \rho_f C_f \tag{3}$$

The fluid flow in the reservoir can be expressed as

$$\phi \frac{\partial \rho_f}{\partial t} + \nabla \cdot (\rho_f \mathbf{q}) = 0 \tag{4}$$

Where **q** (m/s) defines by Darcy's law as:

$$\mathbf{q} = - \frac{k}{\mu} (\nabla P - \rho_f \mathbf{g}) \tag{5}$$

in which *k* is the intrinsic permeability (m²) of the porous medium, μ (Pa.s) is the fluid dynamic viscosity, **g** (m/s²) is the gravity vector, and *P* is the hydraulic pressure (Pa).

The geothermal fluid density and viscosity variation with temperature are based on the exponential functions for the geothermal fluid in the Soultz-sous-Forêts EGS, as described in the following functions according to (Magenet Vincent and Fond, 2014):

Table 1
List of parameters values used for the model in the numerical study [30; 51,52; 77].

Layers Parameters	Lias	Keuper	Muschelkalk	Buntsandstein	Granite	Fault
Thermal Conductivity(W/(m.K))	2.5	1.9	2.3	2.3	3	3
Permeability(m²)	3.7 × 10 ⁻¹⁶	5.5 × 10 ⁻¹⁶	7 × 10 ⁻¹⁶	2.33 × 10 ⁻¹⁵	5.15 × 10 ⁻¹⁵	5.34 × 10 ⁻¹⁴
Porosity	0.04	0.044	0.024	0.096	0.03	0.25
Density(kg/m³)	2390	2390	2390	2390	2630	2630
Heat Capacity(J/(kg.K))	1006	1016	1021	573	828	828

Table 2

List of parameters values' range used for the parametric sensitivity analysis. A full factorial design is carried out resulting in 16,200 reservoir simulations.

Sensitivity Parameter	Values
Well Planar Azimuth (Injection towards Production). Number in the parenthesis shows the rotation angle from original case (SN)	SN (0°), SE (45°), EW (90°), NE (135°), WE (270°)
Well Spacing (Along the fault plane) (m)	600, 800, 1000, 1200
Injection/Production Flow Rate (kg/s)	50, 70 [77], 90, 120, 160
Injection temperature (°C)	50, 70, 90
Fault Permeability (m ²)	5.34 × 10 ⁻¹⁵ , 5.34 × 10 ⁻¹⁴ [30], 5.34 × 10 ⁻¹³
Fault Permeability Anisotropy	- Isotropic - One order of magnitude lower permeability along the strike - One order of magnitude lower permeability along the dip
Perforation Length	- From the top of Buntsandstein to the bottom of the well - Only 150(m) above and below the fault
Subsurface Geothermal Gradient for Muschelkalk and the Lower Layers(K/m)	0.003, 0.0105, 0.018 [30]

$$\rho_T = 1070 \times e \left(-3 \left\{ 1.3224 \times 10^{-4} (T - 293.15) + 43315 \times 10^{-7} (T - 293.15)^2 + 2.49962 \times 10^{-10} (T - 293.15)^3 \right\} \right) \tag{6}$$

$$\mu_T = 1.934 \times 10^{-4} + 61.7 \times 10^{-6} \times e \{ -0.02395 \times (T - 406.4) \} \tag{7}$$

where ρ_T and μ_T are the density (kg/m³) and viscosity (Pa·s) at temperature T respectively. All other fluid properties are assumed to be constant with the specific heat capacity, thermal conductivity, density (at surface) and compressibility set at 3800 (J/(kg·K)), 0.69 (W/(m·K)), 1070 (kg/m³) and 4.5 × 10⁻¹⁰(1/Pa) respectively.

2.3.2. Heat and fluid flow in the fault

In this paper, fault is considered as a 2D object since the fluid flow mainly passes through the fault surface. The flow passing through the normal axis to the fault surface is small and negligible. Fluid flow in the fault is described as [58]:

$$V_F = -\frac{k_F}{\mu} \nabla P_F \tag{8}$$

$$d_F \frac{\partial(\epsilon\rho)}{\partial t} + \nabla \cdot (d_F \rho V_F) = d_F Q_m \tag{9}$$

In which V_F (m/s) is fluid velocity inside the fault. ϵ is the Fault porosity, k_F is fault permeability, and d_F (m) is fault thickness. Q_m is the source or sink term.

2.3.3. Heat and fluid flow in the wellbore

In order to have a computationally efficient model, the wellbores and their surrounding material (cement) are considered as 1D objects so that a significant reduction in the number of mesh elements and consequently on computational time occurs. The mass flow inside the wellbore can simply be considered as a 1D flow, since no flow is occurring perpendicular to wellbore axis. The flow pattern can also be considered as homogeneous front (uniform velocity across the diameter) along the pipe because of the slenderness of the wellbore compared to its length [15]. The mass flow inside the wellbore and the incompressible fluid can be described using the conservation of mass equation:

$$\frac{\partial A \rho_f}{\partial t} + \frac{\partial}{\partial z} (A \rho_f u) = 0 \tag{10}$$

where $A = \pi d_i^2 / 4$ (m²) is the cross-sectional area of the pipe, d_i (m) is the inner pipe diameter, ρ_f (kg/m³) is the density, and u (m/s) is the fluid velocity.

The pressure drop along the wellbore (ΔP^w) can be described as [59]:

$$\Delta P^w = \Delta P_h^w + \Delta P_a^w + \Delta P_f^w \tag{11}$$

in which, ΔP_h^w is the hydrostatic pressure loss, ΔP_a^w is the pressure loss due to acceleration, and ΔP_f^w is the pressure loss due to frictional effects. The pressure loss due to acceleration in a typical reservoir simulation problem is smaller than the heat loss due to gravitation and friction [59]. These terms are defined as [59]:

$$\Delta P_h^w = -\rho g h \sin \theta \tag{12}$$

$$\Delta P_a^w = -\rho_f \frac{\partial u}{\partial t} - \rho_f \frac{\partial^2 u}{\partial z^2} \tag{13}$$

$$\Delta P_f^w = -\frac{1}{2} f_D \frac{\rho_f}{d} |u| u \tag{14}$$

where P (N/m²) stands for pressure, superscript w stands for well, g (m/s²) is the gravitational acceleration, θ is the wellbore inclination angle from the ground surface, and f_D is the Darcy friction factor.

The Darcy friction factor, f_D , is a dimensionless quantity used for the description of friction losses in pipe flow as well as open channel flow. It is a function of the Reynolds number and the surface roughness divided by the hydraulic pipe diameter. Churchill's relation [60], which is valid for the entire range of laminar flow, turbulent flow, and the transient region in between [61], has been used to describe friction in pipes:

$$f_D = 8 \left[\left(\frac{8}{Re} \right)^{12} + (C_A + C_B)^{-1.5} \right]^{1/12} \tag{15}$$

in which C_A and C_B are defined as:

$$C_A = \left[-2.457 \ln \left(\left(\frac{7}{Re} \right)^{0.9} + 0.27 \left(\frac{e}{d} \right) \right) \right]^{16} \quad (16)$$

$$C_B = \left(\frac{37530}{Re} \right)^{16}$$

e (m) is the tubing surface roughness, d (m) is the tubing diameter, and Re is the Reynolds number. Eq (15) shows that the Darcy friction factor is also a function of the fluid properties, through the Reynolds number, defined as:

$$Re = \frac{\rho u d}{\mu} \quad (17)$$

For a low Reynolds number (laminar flow, $Re < 2000$), the friction factor is independent from surface roughness and given by $64/Re$ (Brill and Mukherjee, 1999). In this paper the Haaland equation [62] is used. This formula considers both small and large relative roughness of wells for a wide range of Reynolds numbers ($4000 < Re < 1.1e8$) [63]:

$$\sqrt{\frac{1}{f_D}} = -1.8 \log_{10} \left(\left(\frac{e/d}{3.7} \right)^{1.11} + \left(\frac{6.9}{Re} \right) \right) \quad (18)$$

Heat flow in a wellbore is conductive-convective and arises from the flow of a working fluid running through an inner pipe (tubing), and the thermal interaction between the wellbore components and the surrounding soil mass, plus heat created by friction. It can be all formulated on a 1D heat flow model. Preservation in the equation is made of the involved physical and thermal properties of the pipe components, such as: the cross-sectional areas; the thermal conductivities of the surrounding soil mass and the inner pipe materials; and the fluid thermal properties and flow rate. The 1D representation, implies that the variation of the temperature is along its axis, and that no temperature variation exists in its radial direction. The latter condition is reasonably valid because of the slenderness of the wellbore, where the radial variation of temperature is negligible. Nevertheless, heat fluxes normal to the contact surfaces along the vertical axis are fully considered, and included explicitly in the mathematical model [55]. Hence, the heat transfer inside the wellbore can be defined as:

$$\rho_f A c_{pf} \frac{\partial T_i}{\partial t} + \rho_f A c_{pf} u e \cdot \nabla T_i = \nabla \cdot (A \lambda_f \nabla T_i) + Q_{friction} + Q_{wall} \quad (19)$$

in which T_i describes the temperature in the working fluid, $Q_{friction}$ (W/m) is the heat created by the friction inside the well and Q_{wall} (W/m) describes the heat loss/gain to the surroundings. They are described as

$$Q_{friction} = \frac{1}{2} f_D \frac{\rho A}{d_h} |u| u^2 \quad (20)$$

$$Q_{wall} = (b_{fs}) z (T_s - T_f) \quad (21)$$

$$Z = \pi d \quad (22)$$

where the subscript f represents the geothermal fluid and subscript s represents the surrounding soil mass, b_{fs} (W/m²K) is the reciprocal of the thermal resistance between the fluid and the soil [55]. Z (m) is the contact surface area (perimeter) between the injection well pipe and the surrounding soil formation. Other parameters are similar to those described earlier. In Eq (21), T_s is given by Eq (24) which shows temperature along the wellbore.

2.3.4. Mesh

In order to numerically solve the governing balance equations, pressure and temperature in the reservoir are represented with three-node linear triangular elements for fractures and linear four-node tetrahedral elements for the porous medium. The mesh is refined on the fault plane and around the well perforations where the highest Darcy velocities are expected. A sensitivity of the production temperature results to the mesh refinement and the relative error tolerance is shown in Fig. 2. For the selected mesh, the mesh for the fault plane has a minimum size of 4.5m and a maximum size of 69m and the perforated part of the boreholes has a minimum size of 0.6 m and a maximum size of 39 m. A fixed number of 70 elements is used for the remaining 1D part of the wells. The final mesh depends on the geometry modelled that is conditioned on the position and the spacing of the wells; the mean element count of the batch is 150,800 elements with a standard deviation of 7650 elements.

2.4. Coupling, initial and boundary conditions

At the initial state ($t = 0$) pressure is hydrostatic and temperature follows the thermal gradient as:

$$P_i = P_0 + \rho_f g Z \quad (23)$$

$$T_i = \begin{cases} T_0 + 0.09Z, & Z \geq -1622m \\ T_0 + T_{gradbelowMuschelkalk} Z, & Z < -1662m \end{cases} \quad (24)$$

where P_0 and T_0 are the surface pressure and temperature conditions, taken as 0.1 MPa and 12 °C respectively, ρ_f is the fluid density (kg/m³), g is the gravitational acceleration (m/s²), Z is the domain depth (m) and $T_{gradbelowMuschelkalk}$ is the temperature gradient inside and below the Muschelkalk, with a top contact surface at $-1662m$ (see section 3 for details).

Constant mass flow rate and pressure is applied to the production and injection wells respectively. The cooled fluid is injected by its own weight into the reservoir. The boundary conditions will be defined as follows:

Injection well head pressure is equal to atmospheric pressure as:

$$P_{WH-inj} = P_{atmospheric} \quad (25)$$

Injection bottom-hole pressure is calculated as:

$$P_{BH-Inj} = P_{atmospheric} + P_{hydrostatic} + P_{friction} \quad (26)$$

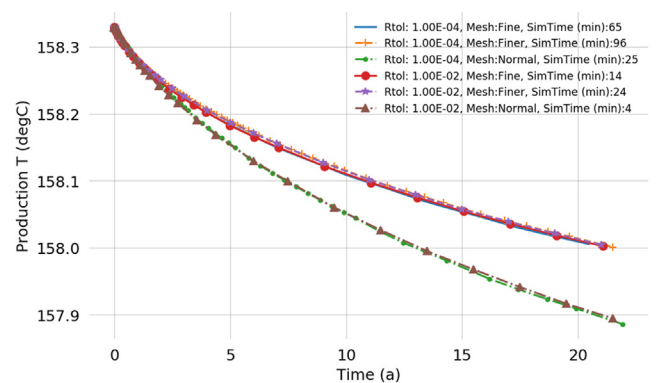


Fig. 2. Sensitivity for the mesh and tolerance selections. Based on these results the selection was made to use a Relative Tolerance of 1e-2 with a fine mesh, resulting in a run time of 14min per simulation using 4 cores on a Xeon E5-1620 v3 processor. It provides a good balance between accuracy of the solution and simulation time.

Injection well head temperature is equal to injection temperature:

$$T_{WH-Inj} = T_{injection} \quad (27)$$

Injection well bottom-hole temperature is derived from the 1D energy balance equation which is solved on the injection well. This temperature will be coupled and placed as boundary condition for the energy balance equation in the reservoir (eq (1)).

$$T_{(injection\ well\ perforation)} = T_{(BH-Inj)} \quad (28)$$

Temperature is integrated over the production perforation, weighted by flowrate at any timestep and placed as a boundary condition for the production well bottom-hole as:

$$T_{BH-Prod} = \int_0^l T \cdot u \quad (29)$$

In which l is the production perforation length and u is the fluid flow rate. Pressure is averaged over the length of production perforation at any time step and placed as a boundary condition at the production well bottom-hole.

$$P_{BH-Prod} = \frac{\int_0^l P \, dl}{\int_0^l dl} \quad (30)$$

The production rate will be imposed as well head boundary condition:

$$u_{WH-Prod} = u_{production\ rate} \quad (31)$$

2.5. Energy and economic model

2.5.1. Energy produced

The power generated from the wells is calculated as

$$PW_{wellst} = \rho_f c_f Q \Delta T_t \quad (33)$$

where ρ_f is the fluid density, c_f is the fluid heat capacity, Q is the volume flow rate (m^3/hr) and ΔT_t is the well head temperature difference between producer and injector at time t . The required pumping energy for the system is calculated as:

$$PW_{pump} = \frac{Q \Delta P}{\eta_{pump}} \quad (32)$$

where Q is the volume flow rate (m^3/hr), ΔP is the pressure difference between the producer and injector well heads and η_{pump} is the efficiency of the pump. The effective power of the system is therefore:

$$PW_{system} = L_{factor} (PW_{wells} - PW_{pump}) \quad (34)$$

where L_{factor} is the load factor.

2.5.2. Economic model

The economic model is based on previously presented work [17]. The well costs are calculated according to Ref. [48]:

$$Cost_{well} = 1.72 \cdot (0.2Z_r^2 + 700Z_r + 25000) \cdot 10^{-6} \quad (35)$$

where Z_r is the measured depth (m) and $Cost$ is in Euro. The Capital Expenditures (CapEx) are calculated as:

$$CapEx_t = Cost_{inj_well} + Cost_{prod_well} + Cost_{pump} Pumps_t \quad (36)$$

where $Cost_{inj_well}$ and $Cost_{prod_well}$ are the costs of the injection and production well as calculated by eq (35), $Cost_{pump}$ is the cost of the pump and $Pumps_t$ is the number of pumps required at time t .

$$OpEx_t = OpEx_{perc} CapEx_t + P_{pump} Elec_{price} \Delta t \quad (37)$$

where $OpEx_{perc}$ is the OpEx percentage of CapEx at time t , $Elec_{price}$ is the price paid for the electricity to run the pumps ($\$/MWh$) and Δt is the time interval over which to calculate expenses (h). The generated income is calculated as:

$$Income_t = PW_{system_t} heat_{price} \Delta t \quad (38)$$

where PW_{system_t} is the system power (MW), $heat_{price}$ is the price for the generated heat ($\$/MWh$) and Δt is the time interval (h). The cash flow and NPV are defined as:

$$CF_t = Income_t - CapEx_t + OpEx_t \quad (39)$$

$$NPV = \sum_{t=0}^n \frac{CF_t}{(1+r)^t} \quad (40)$$

Where CF is the net cash flow, r is the discount rate and t is the number of time intervals. For all results, economic calculations are performed over an interval of 100 days and the annual discount rate is adjusted accordingly. The inputs used for the economic model are summarized in Table 3.

2.6. Analysis

The resource depletion is evaluated with the thermal breakthrough time and the cold front position.

2.6.1. Thermal breakthrough time

In this paper, the thermal breakthrough time is defined as the time (t) where the following criterion is met.

$$T_{prod_t} \leq 0.95 T_{prod_{t=0}} \quad (41)$$

This allows for the normalization of the results and the cross comparison between different production temperatures.

2.6.2. Cold front position

The cold front position can be seen as complementary to the thermal breakthrough data, as it is valuable to know how far along

Table 3
List of inputs for the economic modelling.

Parameters	Value
Pump Electricity	92 $\$/MWh$ [78]
Pump replacement interval	5 yrs
Pump cost	500 k $\$$
Pump efficiency	60%
Load factor	90%
OpEx percentage	5%/yr
Heat price	60 $\$/MWh$ [79]
Discount rate	5%

the well distance has the cold front progressed. The position of the cold front from the injection well was also studied for all simulation runs. The position is studied on the extracted temperature profile over the shortest between the two wells on the fault surface (see lime line in Fig. 4).

In this paper we propose a novel definition of the cold front position between two wells (X_T). The cold front is defined as the location where the reservoir temperature equals the initial production temperature plus the average of the initial temperature difference between the injection and production well, according to:

$$X_T = \left(X \mid T = T_{inj_{t=0}} + \left(\frac{T_{prod_{t=0}} - T_{inj_{t=0}}}{2} \right) \right) \quad (42)$$

In following analysis (X_T) presented as the percentage of well spacing, knowing the start point is always considered at injection well.

3. Results

An extensive sensitivity analysis of the parameters presented in Table 2 is conducted. All combinations of the respective discrete values were considered in a full factorial design. In total, 16200 simulations were performed. The results presented hereafter refer to the full dataset unless otherwise specified. Firstly, the resource depletion and system lifetime are presented. Following, the NPV and generated energy output results are shown.

3.1. Resource depletion

3.1.1. System lifetime

The distribution of the thermal breakthrough time (system lifetime) for all the studied cases, is shown in Fig. 3 for each

parameter and respective parameter values (defined in Table 2). In this figure median is identified with solid horizontal line, the interquartile showed by dotted horizontal lines. The size of each line (the width of each shape) represents frequency. Comparing the median values within the variation range of each parameter it can be concluded that well spacing and production rate have the highest impact on the system lifetime. Well spacing exhibits a narrower distribution and longer lifetimes as the distance between the injector and producer well increases. Therefore, the shorter well spacing of 600 m has a very dominant effect on the system lifetime exhibiting a distribution with a median value of circa 25 years. Conversely the system lifetime is reduced with increasing production rate, while the distribution range becomes wider, expanding over more years. The highest flow rate of 160 kg/s exhibits the narrowest interquartile range with a median value of circa 33 years. High permeability along the fault dip leads to shorter lifetimes (median value of circa 54 years), while an isotropic fault permeability shifts the distribution lower with a median value of 50 years). A high permeability along the fault strike results in a distribution shifted towards longer lifetimes with the highest median value of circa 55 years. The well planar azimuth (WPA) values show relatively similar distribution ranges while being different in the distribution shapes. A WPA of zero degrees shows the highest median value of circa 67 years.

The shortest interquartile range is with a WPA of 45° and 225° (35–100 years) as in these oblique angles buoyancy flow can expand laterally and away from the production well. The widest interquartile range is observed for 270° (median value of circa 50 years) and 90°. In both these cases the wells are oriented along the dip of the fault therefore along the gravity trace on the fault. Buoyancy flow contributes to cold plume reaching the production well (WPA of 90°). This effect is countered when the producer is placed updip (WPA of 270°), slightly shifting the distribution to

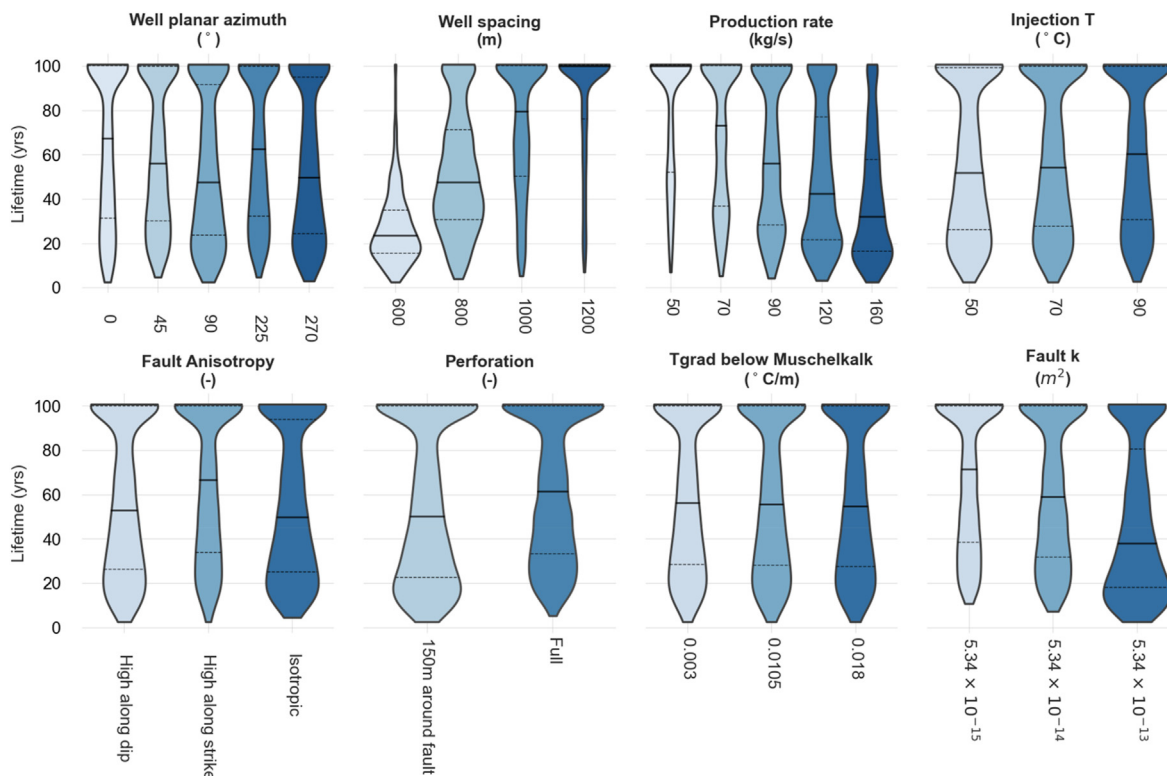


Fig. 3. Distribution of the system lifetime in years for each of the considered parameters and their values, according to eq (40) for the full dataset of 16,200 simulations. The dashed line indicates the median value and the dotted lines the quartiles of the distribution. For simulation where the eq (40) condition is not met, the lifetime is taken equal to 100 years.

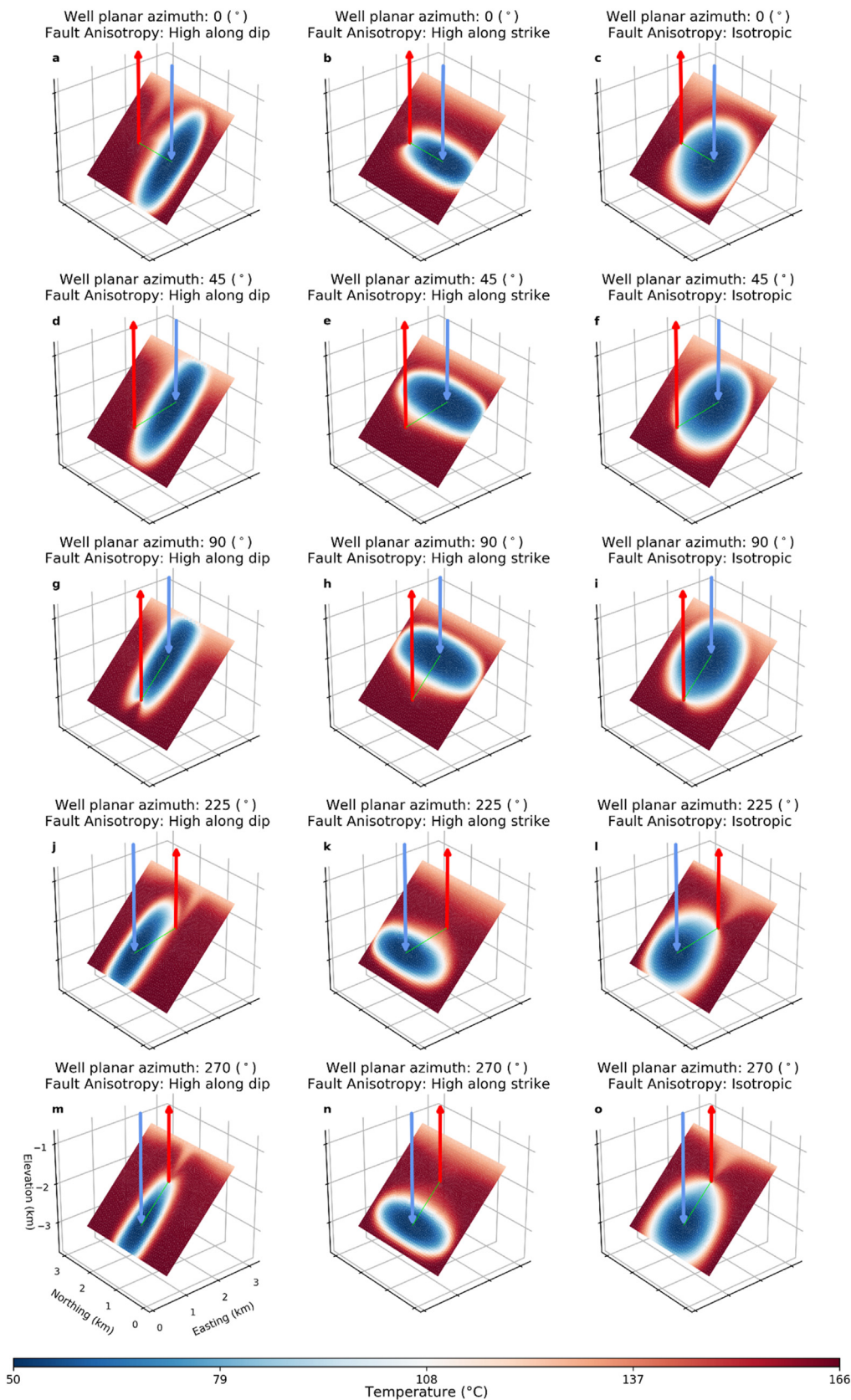


Fig. 4. Temperature distribution on the fault plane after 30 years of production for all the combinations of well planar azimuth and fault anisotropy. The red arrow marks the producer, the blue arrow the injector location and the lime line highlights the shortest distance between the wells on the fault plane (see results in Fig. 6). Data shown have a well spacing of 1200 m (along the fault plane), an injection-production rate of 160 kg/s, an injection temperature of 50 °C, perforation limited to 150 m above and below the fault surface, a temperature gradient below the Muschelkalk of 30 °C/km and a fault permeability of $5.34 \times 10^{-13} \text{ m}^2$.

longer lifetimes compared to a WPA of 90°.

A full perforation length increases the median value and narrows the distribution compared to a perforation limited to 150 m above and below the fault (medians of circa 61 years and 50 years respectively). Increasing fault permeability reduces the median and widens the distribution. This results in a system lifetime to circa 38 years for the highest permeability value of $5.34 \times 10^{-13} \text{ m}^2$. Injection temperature has a minor effect to the overall distribution range, with a slight increase of the lower quartile and median values. Lastly, the temperature gradient below the Muschelkalk has almost no effect to the system lifetime.

3.1.2. WPA and fault permeability anisotropy

When the fault permeability is anisotropic (higher either along the dip or the strike), elongated shapes of the cold plume are observed along the direction of the high anisotropy (Fig. 4). The gravity effect becomes prominent when the producer is positioned shallower (Fig. 4m–o) and the cold plume remains deeper, covering a more restricted area due to its increased density. The opposite effect is observed when the producer well is placed updip (Fig. 4g–i) and gravity aids the colder, denser fluid to reach the producer well. The elongated shape of the cold front is only altered when the WPA is at an oblique angle of 45° or 225° to the direction of the high permeability (Fig. 4d–f and Fig. 4j–l).

For WPA of 0°, 225° and 270°, high permeability along the fault dip leads to fast production along the dip axis (Fig. 4a, j and m respectively) as updip parts of the fault plane with lower temperature contribute to production. The earliest thermal breakthrough would be expected for the WPA of 90° due to gravity contributing to the movement of the cold front towards the producer. When the fault exhibits high permeability along its strike, the cold plume extends mainly along the strike axis (Fig. 4b,e,h,k,n). The cold front propagates further and it partially wraps around the producer well when the orientation of the wells is along the higher fault permeability (Fig. 4b). This suggests that this well configuration would encounter the earliest thermal breakthrough for a high fault permeability along the strike.

An isotropic fault permeability results in a larger fault volume accessible to the wells. As a result the cold water plume does not reach as close to the producer well when the WPA is 0°, 90° or 270° and the fault anisotropy is favourably oriented (Fig. 4b&c, g&i and m&o). However, when the WPA is oblique (45° and 225°) the cold plume reaches closer to the producer well under the isotropic fault permeability compared to the anisotropic cases (Fig. 4d–f and j–l). In these oblique configurations the earliest thermal breakthrough is expected for the isotropic fault permeability, despite the fact that a larger fault area is swept.

3.1.3. Cold front position and production rate

Fig. 5 demonstrates the temperature profile along the shortest distance between the 2 wells for all combinations of fault anisotropies, well planar azimuths, and production rates. In this Fig. 0% is the injector and 100% is the producer location respectively. In all curves in Fig. 5 the cold front shape becomes sharper as the Peclet number (the ratio between convective to conductive heat flow) increases. Conversely, for the lower Peclet numbers (lower flow rate and therefore conductive dominant flow) the front shape becomes more diffusive [37,64].

When the well plane is aligned to the high fault permeability the cold front covers the largest distance, resulting the earliest cold front breakthrough. This is observed for when the fault anisotropy (FA) is high along the strike and the WPA is zero degrees (Fig. 5b) and when the FA is high along the dip and the WPA is 90° and 270° (Fig. 5g,m). The cold front covers the shortest distance when the WPA is perpendicular to the high fault permeability direction. This

is the case when FA is high along dip and the WPA is 0° (Fig. 5a) and when FA is high along the strike and the WPA is 90° or 270° (Fig. 5h,n). For both WPA of 90° and 270° an isotropic FA exhibits results intermediate between the favourable and unfavourable orientation of the well with respect to permeability (Fig. 5i,o). For the oblique WPA of 45° and 225° the differences between the FA orientation is minimized and the isotropic fault exhibits the larger covered distance of the cold front (Fig. 5f,l).

With an isotropic fault and a WPA of 45° the denser cold water is also assisted by gravity and exhibits an earlier thermal breakthrough compared to a WPA of 225°. Between a WPA of 45° and 225° the cold front distance is significantly different for the lower rates, but as the rates increase the density flow effect is minimized and the curves are much more similar. With the producer well positioned updip the higher rates (120 and 160 kg/s) exhibit a distinct dent in the curve around the 75% distance between the wells (Fig. 5i,o). When the WPA is oriented along the fault dip (WPA of 90° and 270°) these differences become even more apparent as the effect of gravity is maximized. All differences are less prominent as the rates are increasing as the effect of density flow becomes less pronounced.

The WPA of 225° and 270° that position the producer updip the temperature curve exhibits levelling off and a very sharp arrival to the production well location, which could be attributed to shallower parts with lower temperature contributing to the production (see also Fig. 4).

The distribution of the cold front position (see eq(43)) along the shortest distance between the wells is shown in Fig. 6. A WPA of 90° the cold front travels the longest distance between the wells, resulting in the highest median value and a distribution closer to the producer. For a WPA of 0° an almost binomial distribution is observed that can be attributed to the favourable or unfavourable WPA orientation to the fault permeability. The WPA of 45° shows an almost uniform distribution suggesting that this orientation is the least sensitive to the changes in other parameters. For both 225° and 270° WPA the shift closer to the injector is a result of the cold front having to travel against gravity towards the updip producer (see also Fig. 4). This effect is stronger for the WPA of 225° that allows the cold water plume to diverge laterally compared to the WPA of 270° where the buoyancy flow might be partly countered by the injector well (see also Fig. 4).

The distance covered by the cold front, after 30 years of simulation, decreases with the increase of well spacing. This can be attributed to two reasons: firstly, due to an increased well spacing increasing the reservoir volume available to the wells and secondly due to the buoyancy flow impact being accentuated with longer well spacing. Similarly, an increasing flow rate shifts the position of the cold front closer to the producer. Both these results are a complementary explanation to the system lifetime (see also Fig. 3).

With increasing injection temperature, the cold front moves closer to the injector due to a smaller temperature difference between the reinjected and the reservoir fluid and less pronounced buoyancy flow. This leads to small increases in the median values and slight shifting of the distribution towards the producer. The cold front propagates the least when a high fault anisotropy along the strike is present (Fig. 6); this effect can be attributed to gravity diverting larger parts of the flow downdip, along the preferential pathway of the permeability anisotropy (see also Fig. 4). Additionally, only one considered WPA is aligned with the high fault anisotropy along the strike.

A complete perforation of reservoir thickness results in more volume available for heat extraction and fluid flow. Accordingly, a slightly shorter interquartile distance and a slight decrease of the cold front position is observed compared to limiting the perforation 150 m above and below the fault plane (Fig. 6). The temperature

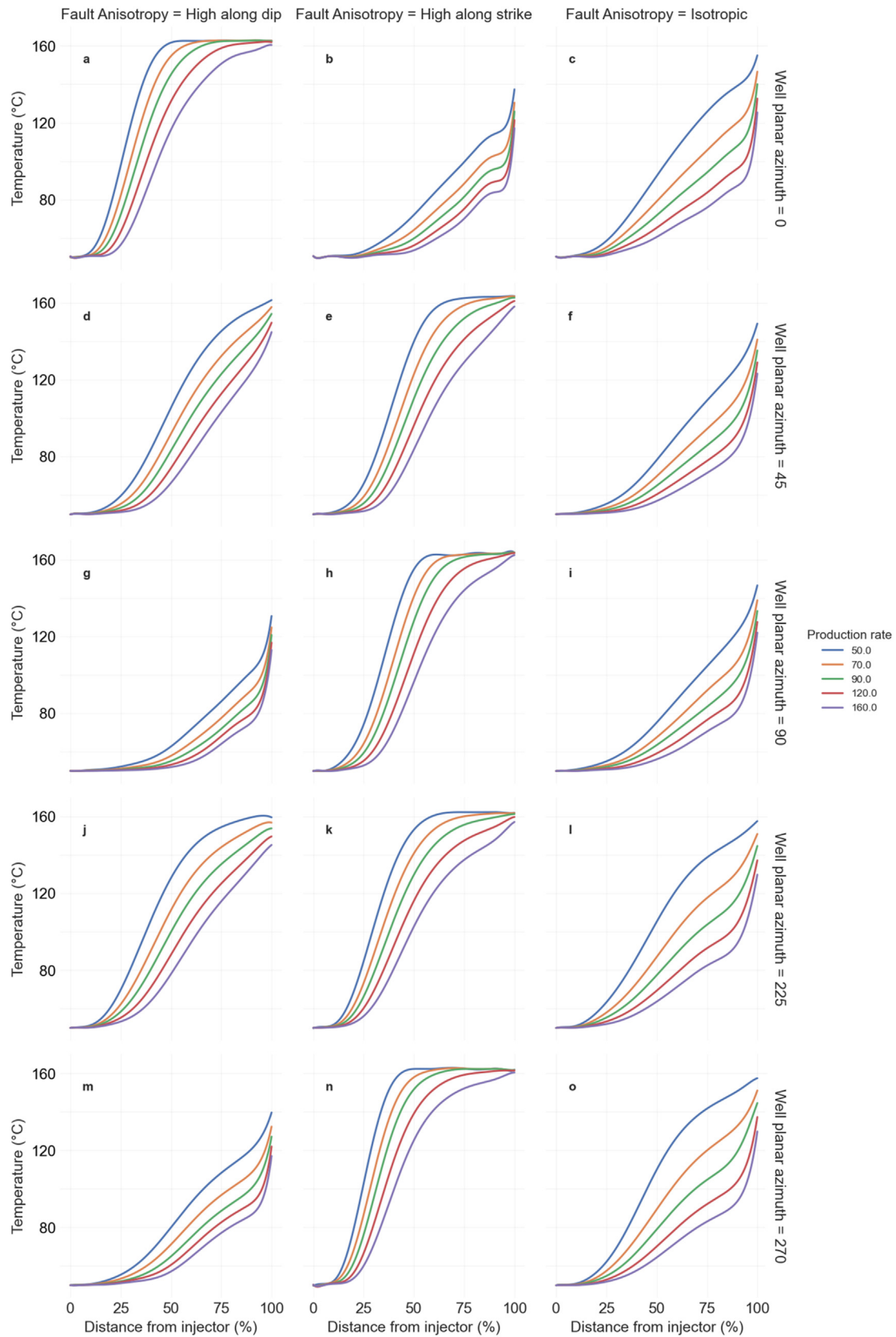


Fig. 5. Temperature profile after 30 years of production along the shortest distance (lime line on Fig. 4) connecting the injector well (0% distance) and the producer well (100%) for all the combinations of rotation, fault anisotropy and injection-production rate. Data shown have a well spacing of 1200 m (along the fault plane), an injection temperature of 50 °C, perforation limited to 150 m above and below the fault surface, a temperature gradient below the Muschelkalk of 30 °C/km and a fault permeability of 5.34×10^{-13} m².

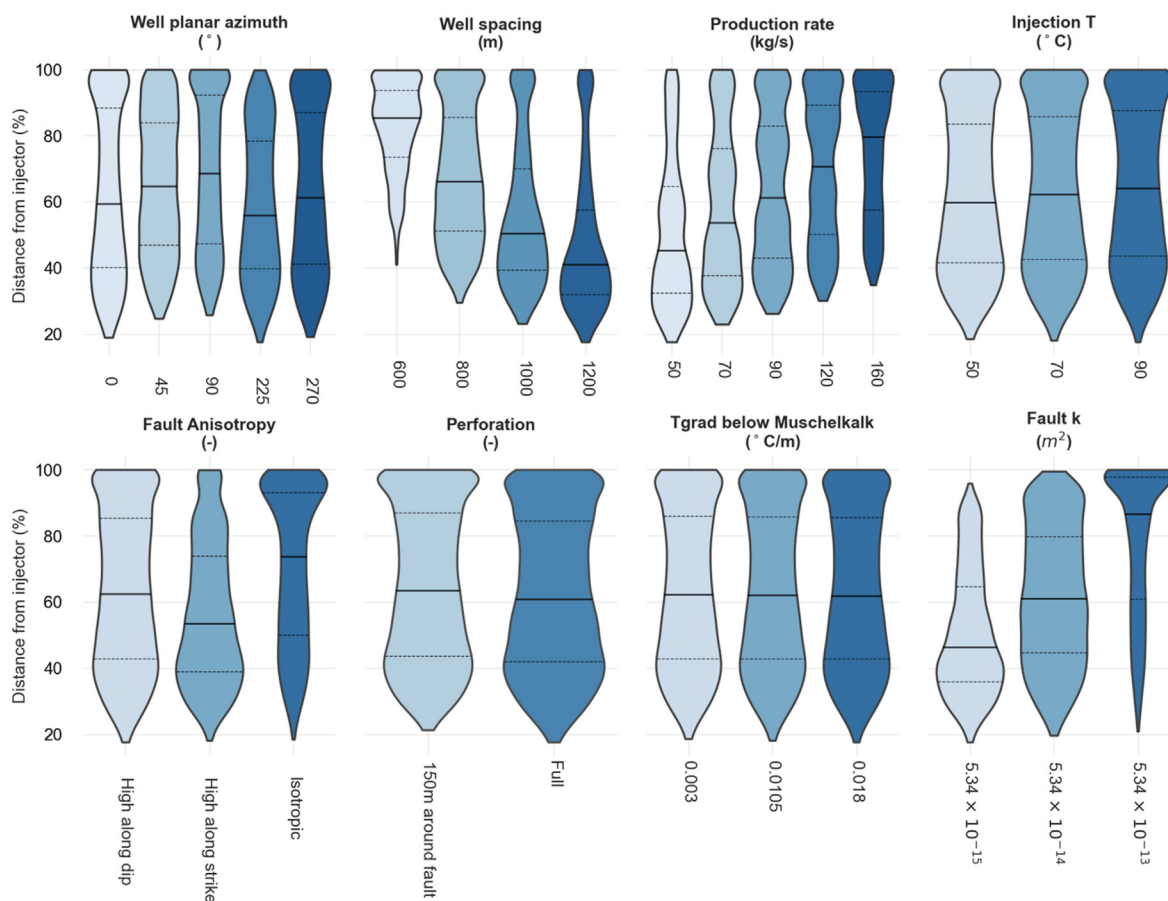


Fig. 6. Distribution of the cold front position (X_r) along the shortest streamline (lime line on Fig. 4) as a percentage of the well spacing for each of the considered parameters and their values, according to eq. (43) for the full dataset of 16,200 simulations after 30 years of simulation. The black line indicates the median value and the dotted lines the quartiles of the distribution.

gradient below the Muschelkalk appears to have no effect on the position of the cold front with almost identical distributions. Lastly, an increasing fault permeability leads to cold front positions closer to the producer and highlights the dominant importance of permeability.

3.2. NPV and produced energy

The sensitivity of the NPV to the model inputs is showcased in Fig. 7. The WPA of 225 shows a slight reduction of the generated NPV, which is more pronounced for the WPA of 270. This decrease can be attributed to the contribution of lower temperature to the production well that is positioned updip (see also Fig. 4m-o and Fig. 5m-o). A WPA of 45° results in the highest median value and a narrower distribution towards lower NPV values. Increasing the well spacing leads to slight increases of the NPV due to extended system lifetime (see Fig. 3) resulting in higher amounts of produced energy. Increasing the well spacing improves the median NPV but also widens the distribution. Therefore, larger well spacing accentuates the influence of other system parameters (see also Fig. 8 and Fig. 12). Similarly, higher rates also lead to wider distribution with the effective change in the distribution width being more pronounced than for changing well spacing. Higher rates also result in increased need for pumping that in turn decreases median NPV values if the conditions are not favourable (see also Fig. 11 and Fig. 12). Injection temperature shows a high impact as more energy can be generated from the same amount of circulated water,

resulting in high values of generated NPV with decreasing injection temperature.

3.2.1. NPV sensitivity to model inputs

The highest median NPV is observed when FA is high along the fault strike. An isotropic FA always results in lower NPV, due to earlier thermal breakthrough (see also Figs. 5 and 12) under most well configurations. The narrowest distribution is encountered when the FA is high along the fault dip. Similar to injection temperature, increased perforation length enables more heat exchange with the layers around the fault, extending system lifetime and thus resulting in higher NPV values. The temperature gradient below the Muschelkalk also shows a positive effect to the NPV with higher gradients, but this effect is less pronounced compared to the injection temperature and the perforation length. Lastly higher fault permeability leads to lower median NPV, due to earlier thermal breakthrough. The distribution is also the widest suggesting that under favourable conditions higher NPV can be achieved.

The relation between system lifetime and NPV is further explored in Fig. 8. In this figure a more concentrated kernel suggests that the effect of other parameters on system lifetime and NPV is weak. Therefore, the variation of other physical and/or operational parameters do not affect the lifetime and generated NPV significantly and sensitivity and uncertainty analysis are of less value.

A well spacing of 600 m and a low production rate of 50 kg/s results in the highest density at about 45 years and an NPV of circa

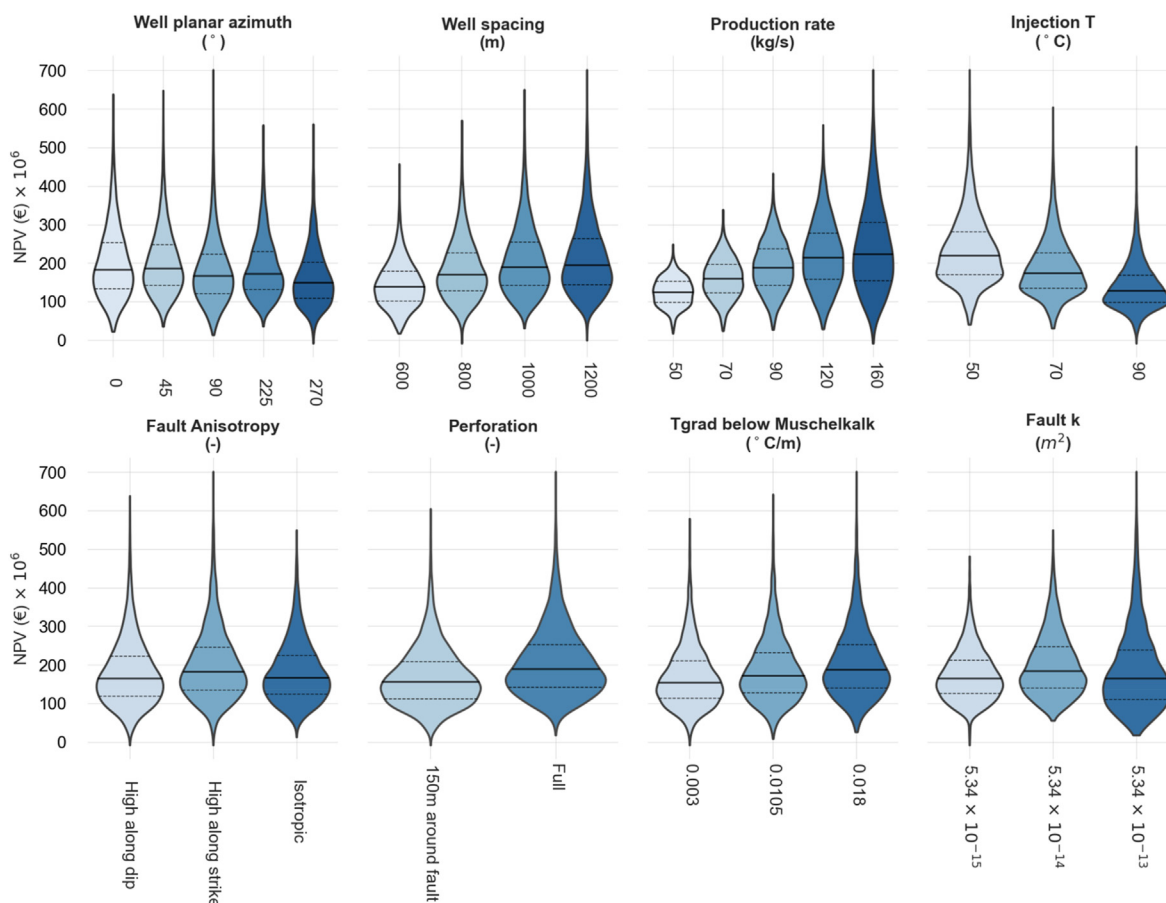


Fig. 7. Distribution of the generated NPV for each of the considered parameters and their values, for the full dataset of 16,200 simulations at the time of thermal breakthrough. The black line indicates the median value and the dotted lines the quartiles of the distribution.

160 M€. Gradually increasing the rates to 70 kg/s and 90 kg/s leads to shorter lifetimes and minor changes of the NPV (Fig. 8b and c). For rates above 120 kg/s system lifetime is reduced while the NPV range widens towards higher and lower values (Fig. 8d and e). With increasing well spacing the distributions shift towards longer lifetimes (Fig. 8f,k,p), while the generated NPV range does not change. With a well spacing of 1200 m no thermal breakthrough (as described in eq (40)) for rates of 50 kg/s or 70 kg/s respectively (Fig. 8p,q).

Considering a rate of 160 kg/s and a well spacing 800m, we observe a strong kernel (Fig. 8j). The largest well spacing and higher rates (1200 m and 160 kg/s respectively, Fig 8t) results in the widest spread in the distribution of both the NPV and the system lifetime and the kernel is not as concentrated. The distribution results in NPV close to zero under some cases, despite the long system lifetimes (see also Fig. 12). This shows that the variation of other parameters impact both the lifetime and NPV significantly. In this scenario, sensitivity and uncertainty analysis over the parameters has utmost importance and its further explored in Fig. 12.

3.2.2. NPV and system lifetime

Changes in the distribution of the generated NPV for the subset of 1200 m well spacing and the high rates of 160 kg/s are further explored in Fig. 9. With regards to the injection temperature the largest changes are observed when the wells are oriented along the strike (WPA of 0°) or when the producer is positioned updip (WPA of 225 and 270). In these cases, the shape of the distribution changes and becomes less wide when the injection temperature is

increased. Increasing the injection temperature has the least negative effect when the producer is positioned downdip (WPA of 45° and 90°). In this case increasing the injection temperature does not alter the distribution shape.

Fault permeability values have the strongest impact when the producer is positioned downdip (WPA of 45° and 90°). For the WPA of 45° and 90° the reduction in fault permeability (regardless of any anisotropy) is enough to alter the NPV distribution from a very wide distribution to a very narrow one as fault permeability is reduced; Therefore, when the producer is downdip the low fault permeability becomes dominating for the NPV. A WPA along the fault strike is the least affected by the permeability of the fault both in terms of mean values but also in distribution shape, meaning that it is the most robust choice under uncertainty of the fault permeability.

A longer perforation length always results in increased generated NPV as it prolongs the production of higher temperatures due to increased heat exchanged with the surroundings formations. The effect is comparable for all WPA without significant changes in the distribution shape between the different perforations.

An increased temperature gradient for the layers below the Muschelkalk also improved the NPV for all considered WPA. The most prominent impact gain is when the WPA are either along the fault strike (WPA of 0°) or the producer is positioned downdip (WPA of 45° and 90°). The reason is that downdip wells are also encountering deeper layers that are more affected by the increased gradient.

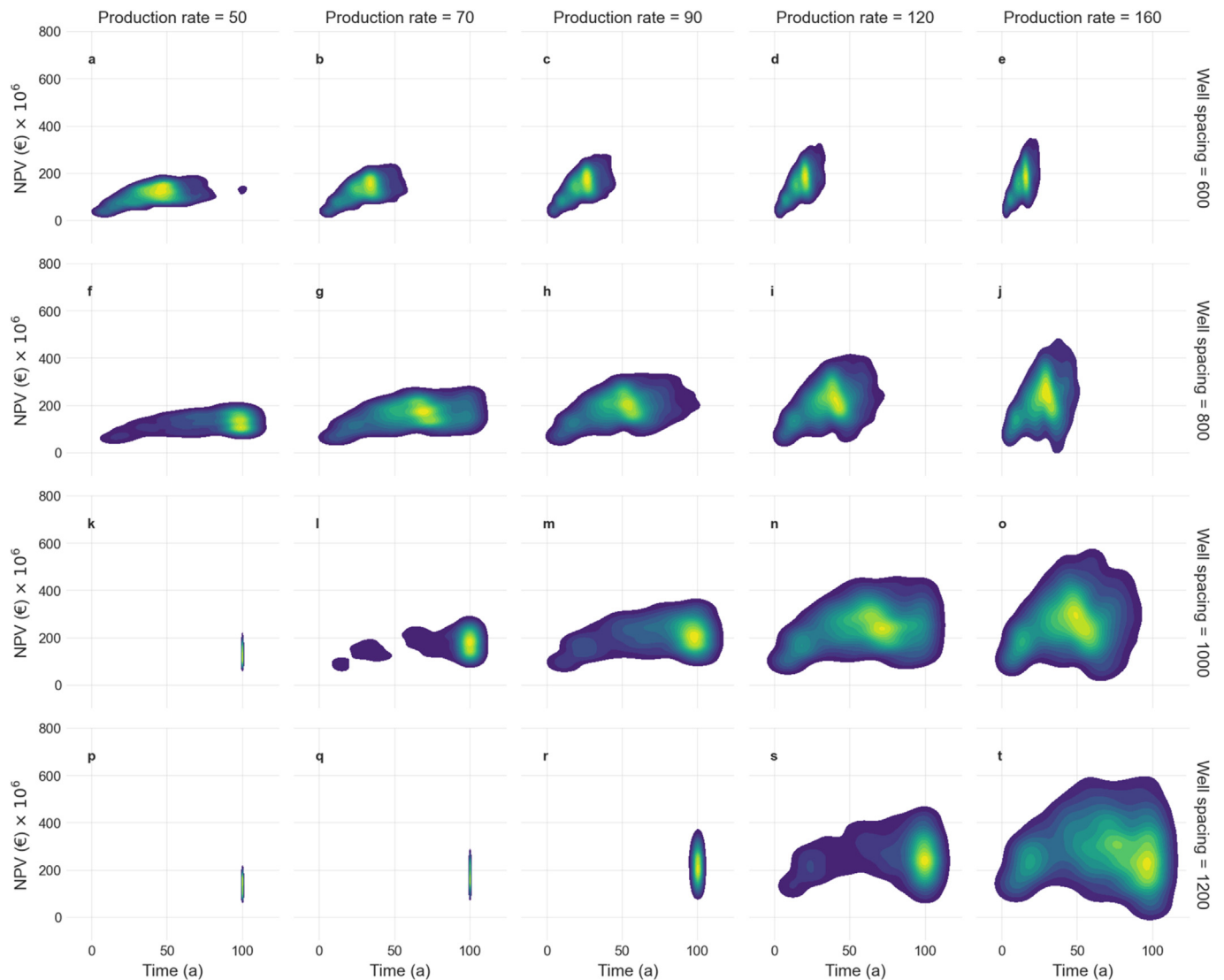


Fig. 8. Kernel density estimation of system lifetime (xaxis) with the generated NPV (yaxis) for the combinations of Rates (columns) and well spacing (rows) for the full dataset of 16,200 simulations. Kernel density estimation is performed per subplot and is therefore not comparable between subplots. In each plot yellow shows high and blue low density.

3.2.3. NPV and WPA

Parameters that improve the efficiency of heat extraction do have a more prominent effect on the produced energy (Fig. 10). Increasing the injection temperature greatly impacts the cumulative energy produced; the impact is negative and more pronounced between 70 °C and 90 °C compared to 50 °C and 70 °C. Similarly, the impact of the temperature gradient below the Muschelkalk is minor but leads to a longer distribution tail towards higher energy production.

Increasing the well spacing and the rate shifts the distribution to larger amounts of generated energy. Nonetheless rates above 70 kg/s showcase very similar median values but with increasingly higher upper quartiles. For the WPA an orientation along the fault strike (WPA of 0°) has the widest distribution, suggesting that in the presence of uncertainties it is the optimal orientation for ensuring larger amounts of produced energy (see also Fig. 9).

Isotropic fault permeability results in the lowest distribution, with high anisotropy along the strike resulting in the higher median and quartile values. Low fault permeability leads to larger amounts of produced energy through the prolonging of the thermal breakthrough. However as seen earlier (Fig. 9) this does not result in higher NPV.

3.2.4. NPV and produced cumulative energy

The relation between the produced amount of energy and the generated NPV is depicted in Fig. 11. While higher rates do result in larger amounts of produced energy this is not directly correlated to the NPV. The required pumping energy is the controlling factor between negative and positive NPV. For rates up to 90 kg/s we see a strong clustering of the data and a linear increase of the NPV with the cumulative produced energy. From 120 kg/s onward the spread in the data increases. Notably, the WPA with the producer wells either along the strike (WPA 0°) or downdip (WPA of 45° and 90°) show a stronger correlation between increased generated energy and increased NPV (Fig. 11e,j,o). For the other WPA orientations the linear increase of NPV with the cumulative produced energy is only maintained with the fault is isotropic (Fig. 11t,y).

3.2.5. Economic efficiency

The ratio between the generated NPV and the cumulative energy produced is analysed in Fig. 12. For well spacing of 600 m increasing the rates always results in an increased ratio. This increase is minimal when the WPA is oriented along the high value of the fault anisotropy (Fig. 12b,g,m). In this case the NPV per produced MWh is already high with low rates and increases only

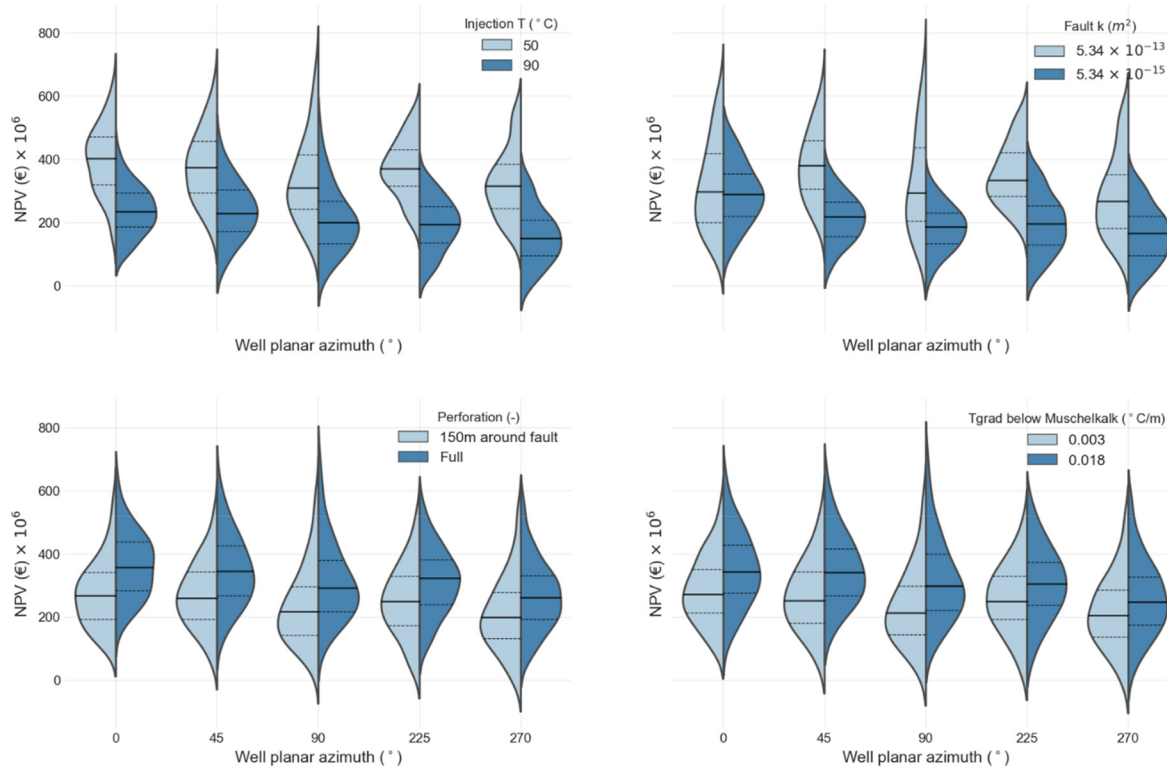


Fig. 9. Distribution of the NPV for each well planar azimuth and the extreme values of injection temperature, fault permeability, perforation and temperature gradient below Muschelkalk for the subset of data with a well spacing of 1200 m and an injection-production rate of 160 kg/s. The black line indicates the median value and the dotted lines the quartiles of the distribution.

slightly with higher rates. With the same well spacing and reducing fault permeability to $5.34 \times 10^{-14} \text{ m}^2$ the NPV per produced MWh increases when the rates increases up to 90 kg/s. Beyond 90 kg/s diminishing returns are encountered: slight increases when the WPA is favourably oriented with respect to the fault anisotropy (Fig. 12g) and reduction of the value per MWh produced when the orientation is unfavourable (Fig. 12b). Further reducing the fault permeability amplifies this impact, therefore, 90 kg/s emerges as an optimum production rate if fault permeability is not the highest.

With a well spacing of 1200 m the NPV per produced MWh exhibits a strong increase with increasing flow rates when the fault permeability is highest and the fault permeability is isotropic. Similarly to the 600 m well spacing, this effect is minimized when the WPA is oriented favourably with respect to anisotropy (Fig. 12b,g,m). Increasing the rates seems to improve the NPV per MWh more when the producer is positioned updip (Fig. 12m). A fault permeability of 5.34×10^{-14} only shows a slight increase of value per MWh under all WPA when the fault permeability is isotropic. For anisotropic fault permeability when the orientation of the WPA is favourable the value per MWh increases with increasing rate, but shows no improvement when increasing the rate from 120 kg/s to 160 kg/s (Fig. 12b,g,m). Lastly, the NPV per MWh for the low fault permeability and the 1200 m well spacing only reduces with increasing rates.

4. Discussion

The results of this study show that - depending on the selected criteria - gauging the general performance of the geothermal reservoirs (lifetime, energy and NPV) results in different (sometimes opposing) outcomes. As shown in Fig. 3, an increase in fault permeability significantly reduces the lifetime of the reservoir

whereas the NPV analysis of the same inputs (Fig. 7) represents a notable increase for higher fault permeability values at favourable operational conditions. This can be explained due to the unfavourable connection between the two wells at higher fault permeability that shortens the system's lifetime whereas the decrease in the required pumping power may lead to more generated NPV. Additionally, the pumping requirements are not high enough to result in NPV reduction, despite the increased pumping pressure needed for the lower permeability (see also Fig. 11).

It is observed that uncertainty in the thermal gradient inside reservoir section has a minor influence on the reservoir lifetime (see Fig. 3) in contrast to its influence on the NPV of the reservoir (see Fig. 7) which is more significant. This effect can be attributed to the importance of the buoyancy effect on the reservoir performance. It is however, noteworthy to mention that larger thermal gradients would be a manifestation of the lower permeability which would impede the natural hydrothermal convection in the system, which can also be linked to the lower NPV in such reservoirs.

The analysis of the Kernel density in Fig. 8 shows that the increase in the injection flow rate for a well spacing of 600 m will reduce the uncertainty associated with the predicted system lifetime. Contrary to this, a longer well distance for a given flow rate results in a broader range in predicted reservoir lifetime (Fig. 8). In the presence of uncertainty with regards to fault permeability and anisotropy, oblique angles prove more resilient for thermal breakthrough compared to directions aligned with the high anisotropy axis (Figs. 5 and 6). This can be a result of the interaction between the higher sweep efficiency with the main flow direction aligned with the lower permeability axis compared to the lower pressure impedance along the higher permeability direction of the anisotropy. Favourable orientation with regards to the anisotropy axis can

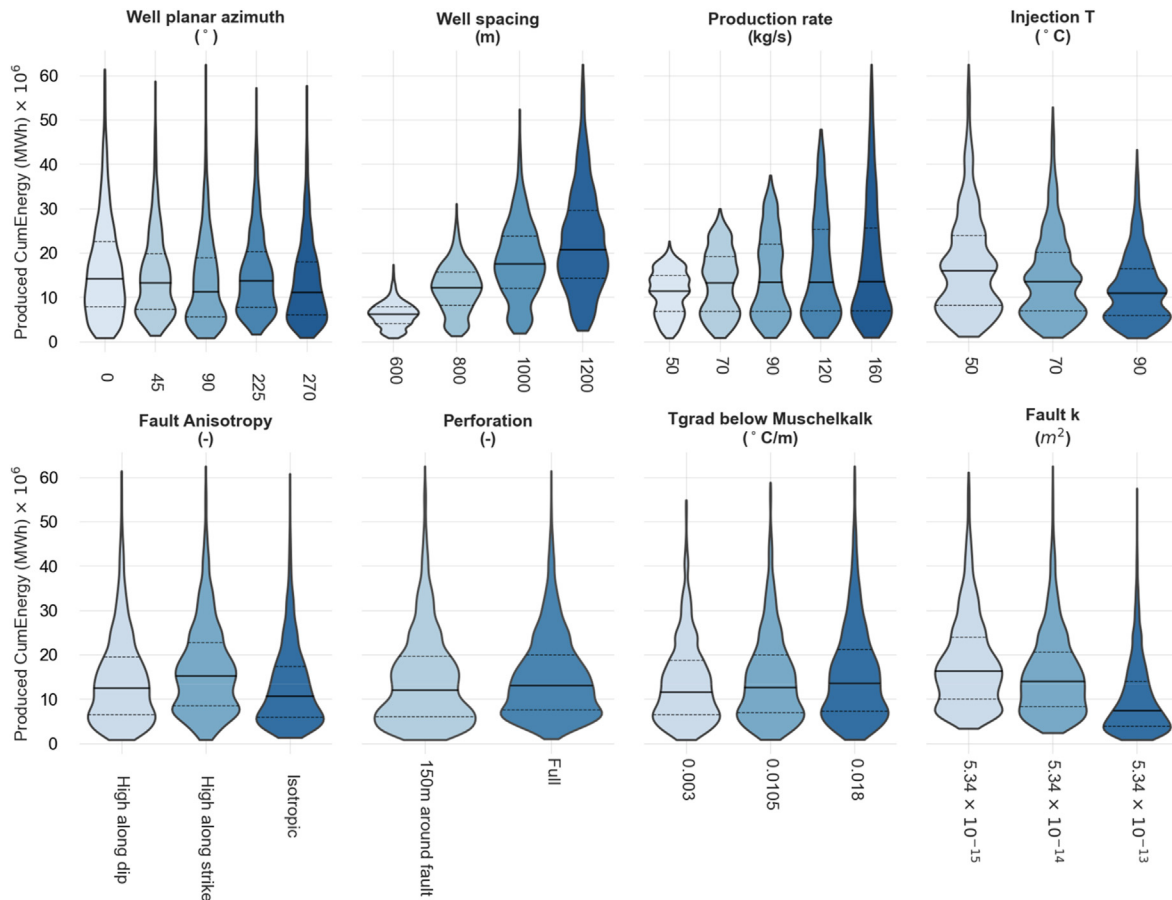


Fig. 10. Distribution of the produced cumulative energy for each of the sensitivity parameters, for the full dataset of 16,200 simulations. The dashed line indicates the median value and the dotted lines the quartiles of the distribution.

be beneficial with regards to NPV (Fig. 7), although it might result in lower system lifetime (Fig. 3). Therefore, initial geological indications of possible fault permeability anisotropy direction can be of critical importance in designing the well configuration. Similar importance to subsurface parameters for techno-economic decisions have been highlighted for EGS projects [65]. Additionally, placement of the production well updip is associated with reduced NPV of the system due to the lower production temperature encountered at shallower depths (Figs. 7 and 9).

Identifying and characterizing the presence of fault anisotropy is crucial for the optimal orientation of the wells with regards to the high permeability anisotropy axis. High fault permeability, regardless of possible anisotropy on the fault, is associated with a significant increase in NPV (Figs. 7 and 9), the uncertainty of which can be further reduced by selecting a proper well placement strategy in terms of orientation (Fig. 9) and spacing (Fig. 8). If characterisation is not possible, results presented herein show that an oblique angle (e.g. WPA of 45° and 225°) is the most robust well configuration strategy to improve the prediction and reduce the uncertainty of NPV, system lifetime and economic efficiency (Fig. 9).

The NPV of the system increases with an increase in production flow rate which is consistent with previous NPV studies of geothermal systems [7,10,17,65]. However, the associated NPV range significantly grows at higher flow rate (see Fig. 8) and higher flow rates can also reduce the economic efficiency when permeability is lower. While higher rates do result in larger amounts of produced energy this is not directly correlated to the NPV (Figs. 8

and 12), as it was previously modelled in faulted hydrothermal systems with formation intervals acting as the main reservoir and fluid pathway [7,66]. Therefore, for systems with the fault plane as the main fluid pathway and in the presence of uncertainty, decreasing the well spacing can lead to a reduced range in the generated NPV, hence increasing decision making confidence (Fig. 12). For shorter well spacing however, it is more important to characterize fault anisotropy compared to when a large well spacing (Fig. 12) is used.

Under the considered uncertainty ranges, there exists an optimum flow rate and well spacing beyond which the economic efficiency of the system can be significantly reduced (Fig. 12). Production rates above 90 kg/s show diminishing returns with regards to the generated NPV in most cases (Fig. 12). Larger well spacing reduces the economic efficiency of the system which decreases with increasing rate for the low permeability cases regardless of well orientation (Fig. 12). Significant improvements in economic efficiency with increasing the production rate above 90 kg/s are only achieved when the wells are oriented favourably with the anisotropy axis that exhibits higher permeability. This improvement prevails also for larger well spacing.

The buoyancy effect is significant at lower flow rates at which the forced convection effects become less dominant. With the highest rates used in our study (160 kg/s) the differences between positioning the producer updip (WPA of 270°) compared to downdip (WPA of 90°) are negligible (Fig. 5). However, these differences are significant for rates up to 90 kg/s and favour the placement of the producer downdip as this combines the effect of

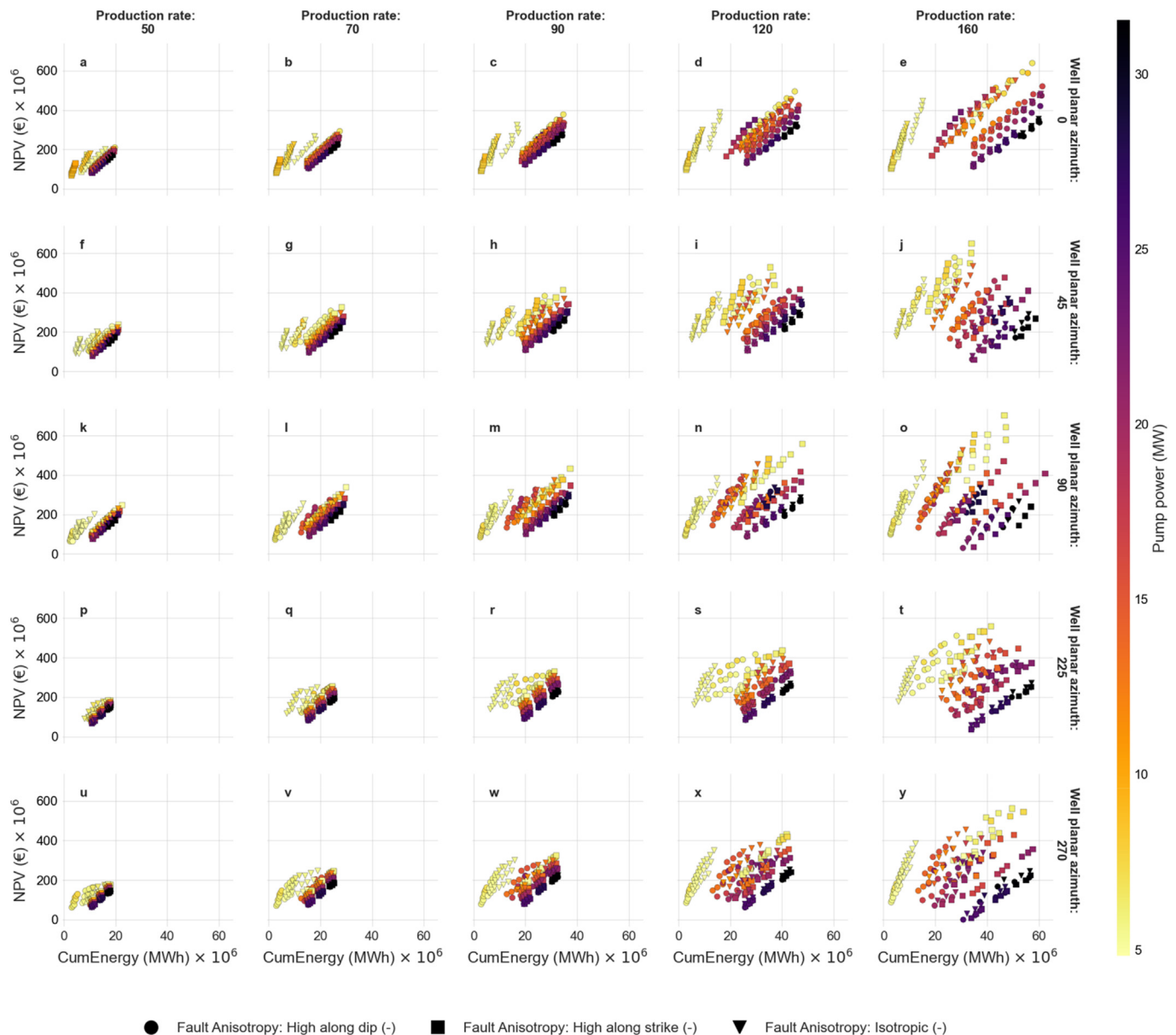


Fig. 11. Cumulative produced energy (MWh) against generated NPV for the combinations of injection and production rates and well planar azimuth. Data is coloured by the required pumping energy and coded according to the fault anisotropy. The dataset is limited to a well spacing of 1200 m.

higher production temperatures due to the geothermal gradient (Figs. 5 and 11). The modelling of the cold front position can inform on how we can better manage the resource when using the fault as the main fluid pathway (Fig. 5). In the case of placing the producer updip, the differences in the cold front position between high and low rates (Fig. 5) aid in identifying the presence and significance of density driven flow in retarding the cold front from reaching the producer well. The results are consistent with the study carried out by Bataillé et al. (2006). While the economic efficiency is reduced, placing the injector well downdip could help with retaining the cold-water plume deeper when low rates are used, therefore prolonging system lifetime (Figs. 4 and 5). In this case, the cooled down plume might exhibit a much larger extent with implications to pressure dissipation and possible fault stability (Fig. 4).

Full factorial design studies such as the one presented here further our understanding of system dynamics under uncertainty, despite the efficient computation design (see section Reservoir

model) remain computationally expensive due to the large number of simulations required (16,200 simulations in this study). Recent advances in reservoir simulation open new possibilities in terms of comprehensive evaluation of uncertainties. The newly presented DARTS simulator is highly efficient [67] in CPU based simulation and is also developed to run on GPU, improving the computation time by 8–10 times [68]. These developments open-up new possibilities for both extensive studies on uncertainty in heterogeneous, fluvial geothermal systems [22] but also for further computational efficiency in optimisation studies [10].

Uncertainty related in the temperature gradient below a certain depth have minor effects on the lifetime but can impact the NPV since they directly affect the produced temperature. Previous studies have highlighted the importance of thermal anomalies [69] and high thermal conductivity of lithostratigraphic layers [70] to the power output of geothermal systems. Our analysis shows that the uncertainty related to the geothermal gradient in this study has

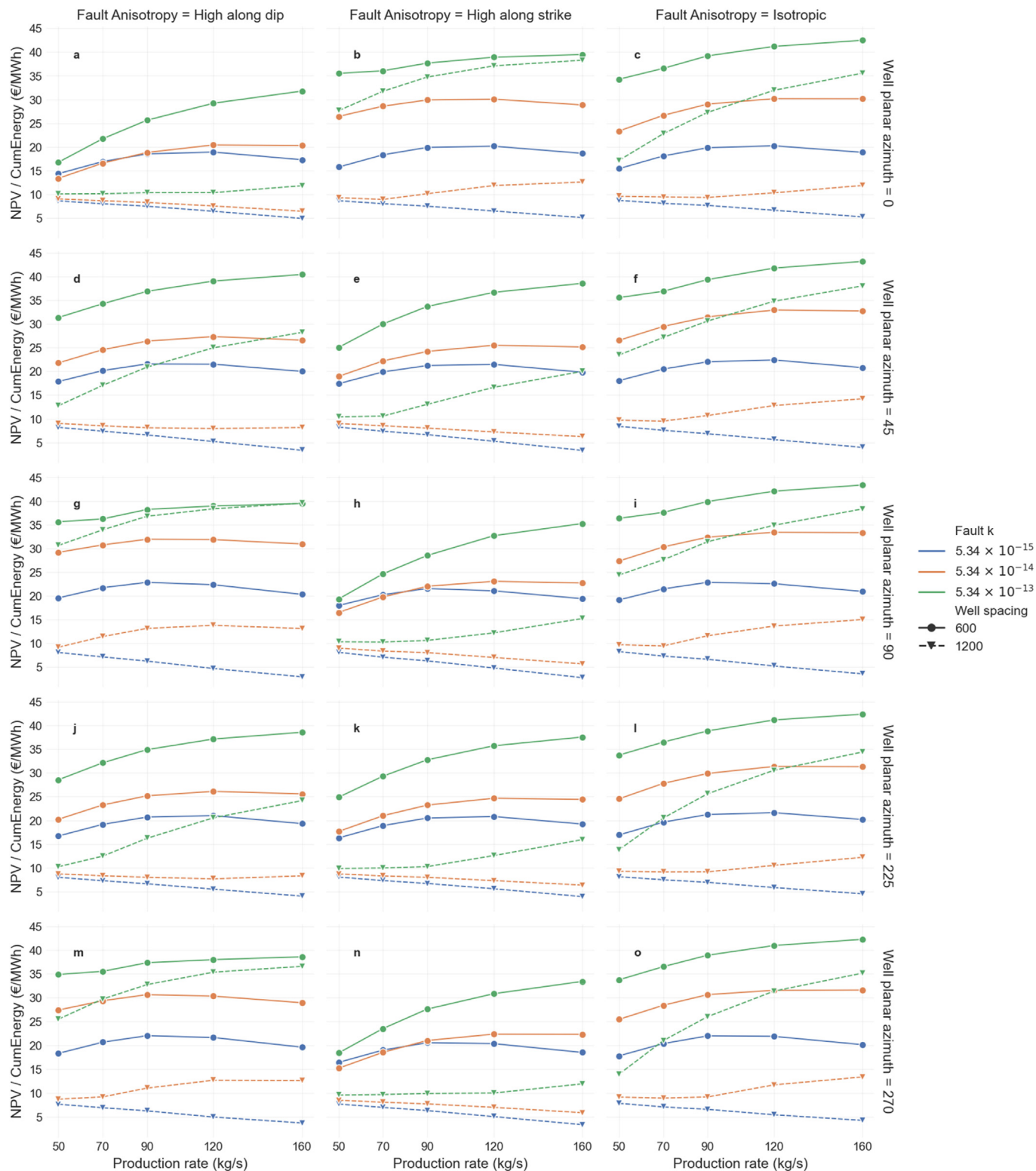


Fig. 12. NPV per cumulative energy produced (€/MWh) against the different flow rates for the combinations of fault anisotropy (columns), well planar azimuth (rows), fault permeability (colour) and well spacing (line/symbol). The dataset shown here uses a perforation limited to 150m above and below the fault, an injection temperature of 50 °C and a temperature gradient below the Muschelkalk of 0.003 °C/m.

almost no effects on the system lifetime and minor effects in the amounts of generated energy and NPV. This can be attributed to the relatively low permeability of the formations and against the much larger permeability of the fault as the main fluid pathway in our

study. The larger permeability of the fault compared with the formation, also imply that the potential hydrothermal convections inside the fault over geological timeframe as well as during the project's lifetime (due to forced circulation) can significantly reduce

the geothermal gradient, and therefore its influence on the overall feasibility of the project. Nevertheless, since the fault has a limited volume compared to a thick formation, the differences become even less significant. Additionally, the uncertainty considered has a small value range and only applies to the lower part of the domain, which further reduces its impact on the system lifetime.

The analysis performed in this work shows that it is important to identify the main anisotropy direction on a fault plane to better position the wells (Figs. 5, Figs. 10 and 12). However, heterogeneity combined with the anisotropy direction should be further explored as the density effects might be affected by spatial heterogeneity patterns. Previous studies on heterogeneity in formation reservoirs have shown significant effects of correlation length [71] and sequencing for the productive layers [7].

The results shown here have not considered the geomechanical effects on the fault and the respective risk implications [72,73]. The pressure distribution on the fault surface in terms of magnitude but also direction could result in energy released in the form of a seismic event which might change the hydraulic properties of the fault [72,73]. Characterisation of these implications in the specific reservoir conditions of the fault acting as the main fluid pathway would require coupled Thermal-Hydraulic-Mechanical (THM) modelling and should be pursued as a follow-up to complement the results presented in this work. While THM modelling is widely used [74,75], it is more computationally expensive and might pose a significant challenge for comprehensive uncertainty assessment as presented in this work.

In this study, no sensitivity was performed with regards to the permeability of the strata intersected by the fault due to the Rittershoffen special geological situation. Notwithstanding, possible high permeable zones might alter the results presented here as the shape and extent of the cold front might be significantly different. Additionally, it is important to also consider the fault angle. A fault angle of 45° was investigated here, however, for thin fluid pathways such as a fault plane steeper angles will accentuate this impact. The quantification of this effect requires an additional study and should be further investigated. Changes in the used fluid density, such as the case of using CO₂ as the geothermal fluid, might further emphasize the relevance of density flow and are not uncommon in geothermal systems [76].

The analysis presented here serves as an exploration of the impact of uncertainties to the geothermal system performance in terms of system lifetime, cold front position, energy output and generated NPV. Nonetheless, the use of a large dataset opens up the possibility to derive mathematical formulations for the above-mentioned indexes. These mathematical formulations will be presented in a follow-up publication.

5. Conclusions

A study is carried out for a geothermal reservoir with the fault plane acting as the main fluid pathway, focusing on the geothermal system performance in terms of lifetime, amount of produced energy and generated NPV. The method presented in this work can inform decision making, improve investment efficiency and outline follow up studies for field development under subsurface and operational uncertainty. Moreover, the method can be generalized and used for different geothermal fields.

Reservoir parameters considered include fault permeability, fault anisotropy and subsurface geothermal gradient, while operational parameters include well positioning, well spacing, flow rate, injection fluid temperature and perforation length. An extended sensitivity analysis is carried out taking into account all discrete combinations of the above-mentioned parameters in a full factorial

design study comprised of 16,200 3D Hydraulic- Thermal (HT) reservoir simulations. The modelled system conceptually represents the Rittershoffen geothermal reservoir (NE France) and is implemented in Finite Element Method (FEM).

Results of this study highlight the importance of the well placement strategy for profitability of geothermal projects by influencing the NPV for given reservoir and operational parameters. Under uncertain conditions, oblique angles (WPA of 45° and 225°) are consistently resulting in higher NPV and should be preferred if characterization of the fault permeability and anisotropy is not present. If fault permeability and anisotropy are known NPV results can be further improved by aligning the wells to the high permeability axis. Positioning of the production well updip leads to reduced energy and NPV despite comparable system lifetime as a result of lower production temperature.

A novel definition of the cold water front is introduced and its analysis shows how to better manage the by monitoring the position of the cold front between the two wells. The WPA, well spacing production rate and fault permeability and anisotropy have significant effects on the cold front position. Conversely, the injection temperature, perforation and temperature gradient in the deeper layers show minor to no effects.

The produced cumulative energy scales more strongly with the increase of well spacing compared to the increase in rates by extending the system lifetime. However, the NPV does not scale accordingly as higher rates and longer well spacing amplifies the effects of other uncertainty parameters, resulting in a wider spread of the generated NPV.

The shorter well spacing is more economically efficient (€/MWh) and scales better with increasing production rates, despite the lower amount of cumulative energy and revenue generated compared to longer well spacing. Diminishing returns are observed above 90 kg/s of production rate with regards to the economic efficiency (€/MWh) and this effect is amplified as the well spacing increases. Above this rate the economic efficiency is either constant or drastically reduced depending on the combination of well configuration and fault permeability.

Permeability values below $5.34 \times 10^{-14} \text{ m}^2$ require more in-depth analysis for well placement and spacing as they can result in significant reductions in economic efficiency. Uncertainty related to the temperature gradient below a depth of 1660 m has minor effects on the lifetime but can impact the NPV since it directly affects the produced temperature.

Funding

This study is partly supported by the DESTRESS project, funded by the European Union's Horizon 2020 research and innovation program under Grant agreement ID 691728. The authors gratefully acknowledge the funding and collaborations within the project community.

Credit author statement

Alexandros Daniilidis: Conceptualization, Methodology, Software, Formal analysis, Investigation, Resources, Data Curation, Writing – original draft, Writing – Review & editing, Visualization, Project administration. **Sanaz Saeid:** Conceptualization, Methodology, Software, Formal analysis, Investigation, Writing – original draft, Writing – Review & editing, visualization. **Nima Gholizadeh Doonechaly:** Conceptualization, Methodology, Software, Formal analysis, Investigation, Writing – original draft, Writing – Review & editing.

Declaration of competing interest

The authors declare that they have no known competing financial interests or personal relationships that could have appeared to influence the work reported in this paper.

Acknowledgments

The authors would like to acknowledge the comments and feedback of our anonymous reviewers that helped improve the final manuscript.

References

- [1] J.E. Onwunalu, L.J. Durlinsky, Application of a particle swarm optimization algorithm for determining optimum well location and type, *Comput. Geosci.* 14 (2010) 183–198, <https://doi.org/10.1007/s10596-009-9142-1>.
- [2] L. Li, B. Jafarpour, M.R. Mohammad-Khaninezhad, A simultaneous perturbation stochastic approximation algorithm for coupled well placement and control optimization under geologic uncertainty, *Comput. Geosci.* 17 (2013) 167–188, <https://doi.org/10.1007/s10596-012-9323-1>.
- [3] A. Larionov, A. Nifantov, V. Itkin, V. Alexandrov, Methodology of optimal well pattern, location and paths in productive formations during oil and gas fields development planning, in: *SPE Russ. Oil Gas Tech. Conf. Exhib.*, vol. 2006, 2006, <https://doi.org/10.2118/104326-MS>.
- [4] A. Ebadat, P. Karimghaee, Well placement optimization according to field production curve using gradient-based control methods through dynamic modeling, *J. Petrol. Sci. Eng.* 100 (2012) 178–188, <https://doi.org/10.1016/j.petrol.2012.08.014>.
- [5] A.A. Kaniyal, G.J. Nathan, J.J. Pincus, The potential role of data-centres in enabling investment in geothermal energy, *Appl. Energy* 98 (2012) 458–466, <https://doi.org/10.1016/j.apenergy.2012.04.009>.
- [6] M. Procesi, B. Cantucci, M. Buttinelli, G. Armezzani, F. Quattrocchi, E. Boschi, Strategic use of the underground in an energy mix plan: synergies among CO₂, CH₄ geological storage and geothermal energy. Latium Region case study (Central Italy), *Appl. Energy* 110 (2013) 104–131, <https://doi.org/10.1016/j.apenergy.2013.03.071>.
- [7] A. Daniilidis, H.M. Nick, D.F. Bruhn, Interdependencies between physical, design and operational parameters for direct use geothermal heat in faulted hydrothermal reservoirs, *Geothermics* 86 (2020) 101806, <https://doi.org/10.1016/j.geothermics.2020.101806>.
- [8] K.P. Norrena, C. V. Deutsch, Automatic determination of well placement subject to geostatistical and economic constraints, *SPE Int. Therm. Oper. Heavy Oil Symp. Int. Horiz. Well Technol. Conf.* (2002).
- [9] S. Akin, M.V. Kok, I. Uraz, Optimization of Well Placement Geothermal Reservoirs Using Artificial Intelligence, 2010, <https://doi.org/10.1016/j.cageo.2009.11.006>.
- [10] A. Daniilidis, M. Khait, S. Saeid, D.F. Bruhn, D. Voskov, A high performance framework for the optimization of geothermal systems, comparing energy production and economic output, in: *Proc. World Geotherm. Congr. 2020, Reykjavik, Iceland, 2020*, pp. 1–10.
- [11] K. Hutchence, J.H. Weston, A.G. Law, L.W. Vigrass, F.W. Jones, Modeling of a liquid phase geothermal doublet system at Regina, Saskatchewan, Canada, *Water Resour. Res.* 22 (1986) 1469–1479, <https://doi.org/10.1029/WR022i010p01469>.
- [12] P. Ungemach, M. Antics, P. Lalos, Sustainable geothermal reservoir management practice, in: *Int. Course EGECE Bus. Semin. Organ. a Success. Dev. a Geotherm. Proj.*, 2009.
- [13] H. Hofmann, T. Babadagli, G. Zimmermann, Hot water generation for oil sands processing from enhanced geothermal systems: process simulation for different hydraulic fracturing scenarios, *Appl. Energy* 113 (2014) 524–547, <https://doi.org/10.1016/j.apenergy.2013.07.060>.
- [14] C.J.L. Willems, H.M. Nick, T. Goense, D.F. Bruhn, The impact of reduction of doublet well spacing on the Net Present Value and the life time of fluvial Hot Sedimentary Aquifer doublets, *Geothermics* 68 (2017) 54–66, <https://doi.org/10.1016/j.geothermics.2017.02.008>.
- [15] S. Saeid, R. Al-Khoury, H.M. Nick, M.A. Hicks, A prototype design model for deep low-enthalpy hydrothermal systems, *Renew. Energy* 77 (2015) 408–422, <https://doi.org/10.1016/j.renene.2014.12.018>.
- [16] D. Reyer, S.L. Philipp, Applicability of failure criteria and empirical relations of mechanical rock properties from outcrop analogue samples for wellbore stability analyses, *Environ. Geotechnol.* 26 (2013) 45.
- [17] A. Daniilidis, B. Alpsoy, R. Herber, Impact of technical and economic uncertainties on the economic performance of a deep geothermal heat system, *Renew. Energy* 114 (2017) 805–816, <https://doi.org/10.1016/j.renene.2017.07.090>.
- [18] J. Limberger, T. Boxem, M. Pluymaekers, D. Bruhn, A. Manzella, P. Calcagno, F. Beekman, S. Cloetingh, J.-D.D. van Wees, Geothermal energy in deep aquifers: a global assessment of the resource base for direct heat utilization, *Renew. Sustain. Energy Rev.* 82 (2018) 961–975, <https://doi.org/10.1016/j.rser.2017.09.084>.
- [19] D. Brown, R. DuTeaux, P. Kruger, D. Swenson, T. Yamaguchi, Fluid circulation and heat extraction from engineered geothermal reservoirs, *Geothermics* 28 (1999) 553–572, [https://doi.org/10.1016/S0375-6505\(99\)00028-0](https://doi.org/10.1016/S0375-6505(99)00028-0).
- [20] P.M. Harris, L.J. Weber, American Association of Petroleum Geologists., SEPM (Society for Sedimentary Geology), Giant Hydrocarbon Reservoirs of the World : from Rocks to Reservoir Characterization and Modeling, AAPG Mem, 2006, <https://doi.org/10.1306/1215872M88247>.
- [21] S.S. Kang, A. Datta-Gupta, W. John Lee, Impact of natural fractures in drainage volume calculations and optimal well placement in tight gas reservoirs, *J. Petrol. Sci. Eng.* 109 (2013) 206–216, <https://doi.org/10.1016/j.petrol.2013.08.024>.
- [22] S. Saeid, Y. Wang, A. Daniilidis, M. Khait, D. Voskov, D.F. Bruhn, Lifetime and energy prediction of geothermal systems: uncertainty analysis in highly heterogeneous geothermal reservoirs (Netherlands), in: *Proc. World Geotherm. Congr. 2020, Reykjavik, Iceland, 2020*, pp. 1–8, <https://pangea.stanford.edu/ERE/db/WGC/papers/WGC/2020/22157.pdf>.
- [23] S. Saeid, N. Gholizadeh-Doonechaly, A. Daniilidis, The influence of physical and operational reservoir parameters on the Well placement strategies in geothermal reservoirs: a case study in Rittershoffen faulted geothermal reservoir, France, in: *EGU Gen. Assem. 2019, Geophysical Research Abstracts*, 2019, <https://meetingorganizer.copernicus.org/EGU2019/EGU2019-16685.pdf>.
- [24] Y. Wang, M. Khait, D. Voskov, S. Saeid, D.F. Bruhn, Benchmark test and sensitivity analysis for Geothermal Applications in The Netherlands, in: *PROCEEDINGS, 44th Work. Geotherm. Reserv. Eng.*, 2019, pp. 1–11, <https://pangea.stanford.edu/ERE/db/GeoConf/papers/SGW/2019/Wang6.pdf>.
- [25] J. Vidal, A. Genter, F. Chopin, Permeable fracture zones in the hard rocks of the geothermal reservoir at Rittershoffen, France, *J. Geophys. Res. Solid Earth*. 122 (2017) 4864–4887, <https://doi.org/10.1002/2017JB014331>.
- [26] V. Maurer, E. Gaucher, M. Grunberg, R. Koepeke, R. Pestourie, N. Cuenot, Seismicity induced during the development of the Rittershoffen geothermal field, France, *Geotherm. Energy*. 8 (2020) 1–31, <https://doi.org/10.1186/s40517-020-0155-2>.
- [27] K. Boyle, M. Zoback, The stress state of the Northwest Geysers, California Geothermal Field, and implications for fault-controlled fluid flow, *Bull. Seismol. Soc. Am.* 104 (2014) 2303–2312, <https://doi.org/10.1785/0120130284>.
- [28] P. Olasolo, M.C. Juárez, M.P. Morales, S. Damico, I.A. Liarte, Enhanced geothermal systems (EGS): a review, *Renew. Sustain. Energy Rev.* 56 (2016) 133–144, <https://doi.org/10.1016/j.rser.2015.11.031>.
- [29] J. Azzola, B. Valley, J. Schmittbuhl, A. Genter, Stress characterization and temporal evolution of borehole failure at the Rittershoffen geothermal project, *Solid Earth* 10 (2019) 1155–1180, <https://doi.org/10.5194/se-10-1155-2019>.
- [30] C. Baujard, A. Genter, E. Dalmais, V. Maurer, R. Hehn, R. Rosillette, J. Vidal, J. Schmittbuhl, Hydrothermal characterization of wells GRT-1 and GRT-2 in Rittershoffen, France: implications on the understanding of natural flow systems in the rhine graben, *Geothermics* 65 (2017) 255–268, <https://doi.org/10.1016/j.geothermics.2016.11.001>.
- [31] E. Jolie, I. Moeck, J.E. Faulds, Quantitative structural-geological exploration of fault-controlled geothermal systems-A case study from the Basin-and-Range Province, Nevada (USA), *Geothermics* 54 (2015) 54–67, <https://doi.org/10.1016/j.geothermics.2014.10.003>.
- [32] K. Anyim, Q. Gan, Fault zone exploitation in geothermal reservoirs: production optimization, permeability evolution and induced seismicity, *Adv. Geotherm. Res.* 4 (2020) 1–12, <https://doi.org/10.26804/ager.2020.01.01>.
- [33] T.L. Gould, A.M. Sarem, others, Infill drilling for incremental recovery, *J. Petrol. Technol.* 41 (1989) 229–237.
- [34] A. Salmachi, M.R. Bonyadi, M. Sayyafzadeh, M. Haghghi, Identification of potential locations for well placement in developed coalbed methane reservoirs, *Int. J. Coal Geol.* 131 (2014) 250–262, <https://doi.org/10.1016/j.coal.2014.06.018>.
- [35] A. Bataillé, P. Genthon, M. Rabinowicz, B. Fritz, Modeling the coupling between free and forced convection in a vertical permeable slot: implications for the heat production of an Enhanced Geothermal System, *Geothermics* (2006), <https://doi.org/10.1016/j.geothermics.2006.11.008>.
- [36] F. Magri, T. Akar, U. Gemici, A. Pekdeger, Deep geothermal groundwater flow in the Seferhisar-Balçova area, Turkey: results from transient numerical simulations of coupled fluid flow and heat transport processes, *Geofluids* 10 (2010) 388–405, <https://doi.org/10.1111/j.1468-8123.2009.00267.x>.
- [37] S. Saeid, R. Al-Khoury, H.M. Nick, F. Barends, Experimental-numerical study of heat flow in deep low-enthalpy geothermal conditions, *Renew. Energy* 62 (2014) 716–730, <https://doi.org/10.1016/j.renene.2013.08.037>.
- [38] R.D. McFarland, H.D. Murphy, Extracting Energy from Hydraulically-Fractured Geothermal Reservoirs, 1976.
- [39] G. Bodvarsson, G.M. Reistad, Forced geohat recovery for moderate temperature uses, *J. Volcanol. Geoth. Res.* 15 (1983) 247–267, [https://doi.org/10.1016/0377-0273\(83\)90102-6](https://doi.org/10.1016/0377-0273(83)90102-6).
- [40] P. Heidinger, J. Dornstädter, A. Fabritius, HDR economic modelling: HDR software, *Geothermics* 35 (2006) 683–710, <https://doi.org/10.1016/j.geothermics.2006.10.005>.
- [41] F.H. Harlow, W.E. Pracht, A theoretical study of geothermal energy extraction, *J. Geophys. Res.* 77 (1972) 7038–7048.
- [42] H.D. Murphy, J.W. Tester, C.O. Grigsby, R.M. Potter, Energy extraction from fractured geothermal reservoirs in low-permeability crystalline rock,

